Testing the Radio-selection Method of Dual Active Galactic Nuclei in the Stripe 82 Field

Arran C. Gross[1] , Hai Fu[1] , A. D. Myers[2], S. G. Djorgovski[3] , Joshua L. Steffen[1] , and J. M. Wrobel[4]

[1] Department of Physics & Astronomy, The University of Iowa, 203 Van Allen Hall, Iowa City, IA 52242, USA; acgross@uiowa.edu
[2] Department of Physics & Astronomy, University of Wyoming, Laramie, WY 82071, USA
[3] California Institute of Technology, 1200 E. California Boulevard, Pasadena, CA 91125, USA
[4] National Radio Astronomy Observatory, P.O. Box O, 1003 Lopezville Road, Socorro, NM 87801, USA

Abstract

We test the merger-induced dual active galactic nuclei (dAGNs) paradigm using a sample of 35 radio galaxy pairs from the Sloan Digital Sky Survey Stripe 82 field. Using Keck optical spectroscopy, we confirm 21 pairs have consistent redshifts, constituting kinematic pairs; the remaining 14 pairs are line-of-sight projections. We classify the optical spectral signatures via emission line ratios, equivalent widths, and excess of radio power above star formation predicted outputs. We find six galaxies are classified as LINERs and seven are AGN/starburst composites. Most of the LINERs are retired galaxies, while the composites likely have AGN contribution. All of the kinematic pairs exhibit radio power more than $10\times$ above the level expected from just star formation, suggestive of a radio AGN contribution. We also analyze high-resolution ($0.''3$) imaging at 6 GHz from the NSF's Karl G. Jansky Very Large Array for 17 of the kinematic pairs. We find six pairs (two new, four previously known) host two separate radio cores, confirming their status as dAGNs. The remaining 11 pairs contain single AGNs, with most exhibiting prominent jets/lobes overlapping their companion. Our final census indicates a dAGN duty cycle slightly higher than predictions of purely stochastic fueling, although a larger sample (potentially culled from VLASS) is needed to fully address the dAGN fraction. We conclude that while dAGNs in the Stripe 82 field are rare, the merger process plays some role in their triggering and it facilitates low to moderate levels of accretion.

Unified Astronomy Thesaurus concepts: Active galaxies (17); Interacting galaxies (802); Active galactic nuclei (16)

Supporting material: data behind figure, figure sets

1. Introduction

The galaxies of the present-day universe have been built up hierarchically from a series of major and minor mergers. For galaxies like our Milky Way, cosmological hydrodynamical simulations have shown that large components of their material have come from several other galaxies throughout their evolution (e.g., Rodriguez-Gomez et al. 2016; Pillepich et al. 2017). Aside from acquiring more mass, the ensuing gravitational torques can induce stellar bars that drive large amounts of interstellar gas to the central kiloparsec on short timescales (Di Matteo et al. 2005). Inflowing gas from outer regions of the galaxy can supply the pristine raw material needed to induce an intense period of star formation (Barnes & Hernquist 1996; Ellison et al. 2008; Scudder et al. 2012), while also diluting the metallicity of the interstellar medium (Torrey et al. 2012). Most dramatically, the influx of gas streaming toward the nuclear region can trigger supermassive black hole (SMBH) accretion in the central parsec of a galaxy, initiating an active galactic nucleus (AGN; e.g., Barnes & Hernquist 1991; Capelo & Dotti 2016). These active black holes are the most powerful and luminous engines in the universe, at times dominating the luminosity of the host galaxy.

Since SMBHs can be fueled by gas inflows, and inflows can be triggered via tidal interactions during a galactic merger, we might expect there to be AGNs triggered in both merging galaxies at the same time resulting in a dual AGN (dAGN).

Simulations of major galaxy mergers do indicate that simultaneous SMBH accretion could occur if prompted by strong tidal forces during the close approach of a merger (galactic separations $\lesssim 10$ kpc; e.g., Wassenhove et al. 2012; Blecha et al. 2013; Rosas-Guevara et al. 2019). For major mergers, the window for observing a dAGN may be as long as $10-100$ Myr, where the level of activity is likely highest (and thus easiest to observe) during late pericenter passages (Capelo et al. 2017). Recent semi-analytical model simulations by Li et al. (2021) indicate that scales of $\sim 0.3-0.5$ kpc are the most likely separations at which to find dAGNs. At this stage, the merging galaxies should each exhibit an AGN before the final coalescence.

Previous searches for dAGNs have turned up a sparse population of candidates and rigorously confirmed duals (e.g., Satyapal et al. 2017; De Rosa et al. 2019, and references therein). More recently, high-resolution radio imaging has revealed a dearth of dAGNs, including J1502+1115 (Fu et al. 2011) and J1010+1413 (Goulding et al. 2019), while X-ray and optical evidence has uncovered a dAGN in Mrk 739 (Koss et al. 2011; Tubín et al. 2021). A triple AGN system has even been serendipitously discovered at $z = 0.077$ (Pfeifle et al. 2019). At substantially higher redshift than any previously known dAGN, a study using the Dark Energy Survey gives evidence of kiloparsec-scale dual quasars at $z = 5.66$ (Yue et al. 2021). Substantial efforts toward systematic identification of dAGNs have been conducted recently via sweeping optical campaigns (Hou et al. 2020; Shen et al. 2021; Zhang et al. 2021a, 2021b). However, these inhomogeneously selected samples have yielded a modest trove of confirmed dAGNs

(∼50 pairs), suggesting that dAGNs might be intrinsically rare occurrences.

Using a combination of optical spectroscopy and radio imaging, we have conducted a systematic search for dAGNs through a series of three studies. We first identified dAGN candidates within the 92 deg^2 covered by the wide-area 2″ resolution VLA 1.4 GHz survey of the Stripe 82 field (Fu et al. 2015a, hereafter Paper I). Out of ∼18,000 discrete radio sources, we identified 52 candidate pairs that show good positional alignments between the radio sources and their optical counterparts. Optical spectroscopy available for eight of these candidates at that time revealed six pairs with consistent redshifts. We then followed up on these candidates with a pilot study utilizing 0″3 resolution VLA 6 GHz observations (Fu et al. 2015b, hereafter Paper II). The higher resolution radio imaging revealed two of these candidate pairs to be projections of jets from one source overlapping with its companion galaxy. The remaining four pairs were confirmed as dAGNs with compact (≲0″4) nuclear radio emission and core luminosities between $37.3 < \log L_{5\,\mathrm{GHz}}/\mathrm{erg\ s}^{-1} < 39.4$. Follow-up Chandra X-ray observations in our third study revealed that only one of these dAGNs exhibited detectable dual X-ray cores (Gross et al. 2019, hereafter Paper III), relieving the low degree of obscuration within the galaxies and the intrinsically low level of accretion in their cores ($39.8 < \log L_X/\mathrm{erg\ s}^{-1} < 42.0$).

In this fourth installment in the series, we present observational evidence of dAGN activity for a sample of candidates constituting the bulk of the remaining well-aligned pairs. We obtain and analyze optical spectra for 35 pairs (27 new pairs) out of the original 52 to determine which are indeed in kinematic pairs. Through a combination of further Very Large Array (VLA) imaging and optical emission line diagnostics, we rigorously confirm several additional dAGNs, and dismiss many as jetted imposters. Our final census of dAGNs and single AGNs in mergers within the Stripe 82 field allows us to speculate on whether the dAGN duty cycle is in fact enhanced as predicted, indicating the role of mergers in fueling dAGN activity. We also reflect on the effectiveness of our selection strategy in culling samples of dAGN candidates from future large-area surveys. Throughout, we adopt a Lambda cold dark matter cosmology with $\Omega_m = 0.3$, $\Omega_\Lambda = 0.7$, and $h = 0.7$.

2. Observations and Reduction

Our first step in verifying a sample of dAGNs is to ensure that both galaxies in a candidate pair are indeed a kinematic pair at the same comoving distance. Optical spectroscopy of the target pair can be used to not only measure the redshifts, but also to diagnose nuclear activity through spectral emission lines. In Paper I, we analyzed a subset of candidate dAGN systems out of the total 52 grade A and B pairs. These pairs each contain two optical sources that are well matched to radio sources, with good agreement between the position angles; however, the grade B pairs have radio morphologies that might be due to extended radio emission from a single source. Many of these systems had spectra from the Sloan Digital Sky Survey (SDSS) DR10 (Ahn et al. 2014), although spectroscopic coverage for many of the pairs was incomplete because small angular separations result in fiber collisions for fibers closer than 55″ and 62″ for SDSS and BOSS, respectively (Dawson et al. 2013). The pilot sample of eight dAGN candidate systems

was thus a mixture of SDSS archival spectra and new observations using the Keck Observatory.

Of the remaining 44 candidate systems, 13 were chosen to not be observed based on r-band magnitudes, and five observed pairs proved to be too faint to yield sufficiently high signal-to-noise ratio (S/N) spectra and so are not included in the sample. Here, we detail the remainder of the candidate sample: new optical spectroscopic observations of 27 candidate pairs. We also reanalyze the previous eight pairs[5] in a homogeneous fashion with the new observations for a total sample of 35 pairs. For three of the previously confirmed pairs without Keck observations, we default to using the archival SDSS spectra but update our analysis.

2.1. Keck/LRIS Spectroscopy

For the sample of objects lacking complete spectroscopic coverage from SDSS, spectroscopic data were acquired over three observational campaigns between 2015 and 2017. All observations were carried out using the Low Resolution Imaging Spectrometer (LRIS) at the Keck I Observatory (Oke et al. 1995). A 1″5 wide long slit and 560 dichroic were used for all observations. Over the eight different nights of observations, we used the B600 blue grism paired with either the R400 or R600 red grating, although the same setup was used consistently throughout a given night. This leads to varying amounts of overlap between the red and blue sides of the spectra from one night to the next. The details of the optical observations are separated by night in Table 1.

We reduce the raw spectroscopic data using an IDL pipeline tailor-made for LRIS single-slit observations: LPIPE (Perley 2019). Briefly, the pipeline handles the red and blue channels separately, starting with an automated subtraction of flats, cosmic rays, and sky lines. Bright sources in the cleaned 2D spectrum are then used to calculate a generic function for the *trace* using polynomial fitting. While the pipeline can automatically identify objects in the spectra for extraction, this step is handled interactively through a user interface. We isolate the peak of the 1D collapsed brightness profile for each source in a pair separately, and cross-correlation is done between the red and blue channels to check for astrometric consistency. Simple extraction using the trace function is then done to extract the collapsed 1D spectrum of wavelength (pixels) versus counts. Wavelength calibration is done using a pattern matching algorithm on the arc spectra to solve for the polynomial conversion from pixels to wavelength. This solution is tweaked to correct for instrument flexure using a catalog of sky lines. We show an example of the reduction procedure up to this point in Figure 1. Diagnostic figures for the remainder of the sample are included in the online material. These diagnostic plots are useful for redshift identification, which we later refine during spectral fitting.

Finally, flux calibration is performed using spectra of standard stars that are reduced in conjunction with the science spectra. For most nights, either the standard star BD+28 4211 or G191-B2B was observed; Hiltner600 was observed during observations on 15-9-14. The sensitivity function for each night is then derived from the standard stars, accounting for telluric absorption and wavelength-dependent attenuation due to

---

[5] We also reanalyze J2252+0106, which is grade D (offset between an optical and radio source and thus misaligned position angles), but shows obvious signs of tidal interactions from an ongoing merger and is thus of interest.

Table 1
Keck/LRIS Spectroscopic Observations

Designation	r_1; r_2	Slit P.A. (deg)	Exp. (s)
2011-10-23 B600/4000 R400/8500			
0152−0010	16.1; 19.0	51	600
2220+0058	18.5; 19.5	76	600
2232+0012	19.8; 19.1	120	900
2252+0106	15.3; ⋯	90	600
2300−0005	17.4; 17.2	155	600
2302−0003	21.3; 20.6	65	1800
2318+0045	23.1; 20.6	120	900
2014-09-27 B600/4000 R400/8500			
2235+0003	21.6; 22.7	272	1800
2242+0030	23.3; 19.9	295	1800
2015-09-14 B600/4000 R600/7500			
0135+0119	18.4; 22.0	3	2400
0144−0042	22.4; 19.7	334	2400
0152−0010	16.1; 19.0	57	1200
0210−0051	19.6; 21.5	322	2100
2235+0003	21.6; 22.7	273	3600
2258+0030	18.4; 20.5*	234	2400
2305+0024	21.1; 20.0	349	2400
2319+0038	22.0; 20.8	342	1200
2015-10-16 B600/4000 R600/7500			
0111−0000	22.9; 21.0	333	1800
0147−0008	20.7; 20.1	32	1800
0149−0014	19.1; 20.0	354	1700
2244+0010	22.1; 22.6	77	1820
2305+0024	21.1; 20.0	350	1200
2016-09-7 B600/4000 R600/7500			
0120−0046	23.3; 21.0	302	2400
0142−0001	22.5; 21.9	285	1800
0203−0033	22.9; 22.0	191	1200
2211+0027	24.0; 19.6	333	1200
2213+0048	23.9; 21.6	249	1200
2218+0045	23.0**; 22.3	205	2400
2229−0004	22.6*; 23.0	268	2400
2245+0058	20.4; 23.0**	313	2400
2250+0011	23.3; 21.9	191	2400
2303−0117	21.7; 20.3	254	1200
2308+0025	23.4; 20.9	191	2400
2017-05-31 B600/4000 R400/8500			
2242+0030	23.3; 19.9	295	3600
2017-06-23 B600/4000 R400/8500			
2304−0109	23.0**; 23.3**	49	4800
2017-10-15 B600/4000 R400/8500			
0116+0058	23.0; 24.0**	355	2400

Note. Observation log for the Keck/LRIS targets. Observations are grouped by night (in bold), where we also specify the blue grism and red grating used. We give the J200 designation for the target galaxy pair, the SDSS r-band AB magnitudes for the two targets in each pair, slit position angle in degrees east of north, and exposure time. Instances where a target lacks r-band photometry, we quote the SDSS g-band or i-band magnitude (denoted with * and **, respectively). Sources without photometric data are marked with ⋯.

differential airmass between the standard star and science observations. After applying the sensitivity function to the science spectra, the red and blue channels are joined together at the point where there is minimal difference between the red and blue sensitivity functions. For the sources previously reduced

in Paper I, we obtain consistent data products using LPIPE. Some sources were observed on multiple nights resulting in duplicate reduced spectra. In these cases, we default to the data with higher S/N, which is found for the observations with longer exposure time. We note which observation is used for the remainder of our discussion in Tables 2 and 3.

As a first step in estimating redshifts, we use the non-flux-calibrated spectra since emission and absorption features are generally more dramatic and identifiable before calibration. We do also compare against the fluxed spectra to check for emission lines hidden by the telluric absorption bands. In the lower panels of Figure 1, we show a suite of nebular emission lines and stellar absorption features using vertical lines, whose values are taken from NIST.[6] In most cases, there is at least one clearly identifiable emission or absorption marker in both objects in a given pair, in both red and blue channels of the spectrum. We also indicate more prominent spectral features in the 2D spectra in the upper right panels of Figure 1. In general, the quality of the LRIS data allows us to obtain reliable estimates down to roughly $z \pm 0.0001$, such that a shift in either direction on the binned spectrum would lead to an obvious mismatch between the binned peaks and the known locations of the constellation of emission and absorption lines. We obtain a more rigorous estimate of the uncertainty on z during our subsequent spectral fitting.

The redshift values allow us to separate our sample into two populations: kinematic galaxy pairs with consistent redshifts ($\frac{\Delta z}{1 + z} \lesssim 0.0017$), and projected pairs with large redshift differences. We give the redshift estimates for these sub-samples in the legends of the diagnostic figures. Complications with the by-eye estimate arise in cases of low S/N spectra. The most likely issue seen is that the blue side of the spectrum is faint (peak source counts <150 per spectral bin), even if the red side is very bright. This is not surprising given that many of our targets are intrinsically red in their SDSS optical co-add images. We can still obtain a redshift estimate, although we flag the less certain measurements to denote these complications. The majority of our sample has easily discernible redshifts, and hence are not assigned a flag (64% = 45/70 objects). We give our demarcations for the quality of redshift estimate as flags in Tables 2 and 3 in order of decreasing certainty as (moderate) the blue side may be faint, but obvious markers can still be seen in the red side of the spectrum; (fair) both sides of the spectrum might be faint or noisy or contain an uncleaned cosmic, but there is still somewhat obvious complexes of features that match up; (poor) the spectrum is so faint or noisy that we resort to template matching on a binned version of the spectrum. Only one object in the kinematic pairs sample falls into this last flagged category.

In total, we find 21 kinematic pairs and 14 projected pairs. The kinematic pairs generally have $\Delta V \lesssim 500\,\mathrm{km\,s^{-1}}$. Four pairs exceed this loose restriction: J0147−0008 ($\Delta V = 1148\,\mathrm{km\,s^{-1}}$), J2229−0004 ($\Delta V = 775\,\mathrm{km\,s^{-1}}$), J2258+0030 ($\Delta V = 658\,\mathrm{km\,s^{-1}}$), and J2319+0038 ($\Delta V = 894\,\mathrm{km\,s^{-1}}$). While we do not focus on the projected pairs during the remainder of this text, they could constitute a useful sample for studying the reddening effects between foreground and background galaxies, or perhaps gravitational lensing at moderate redshift.
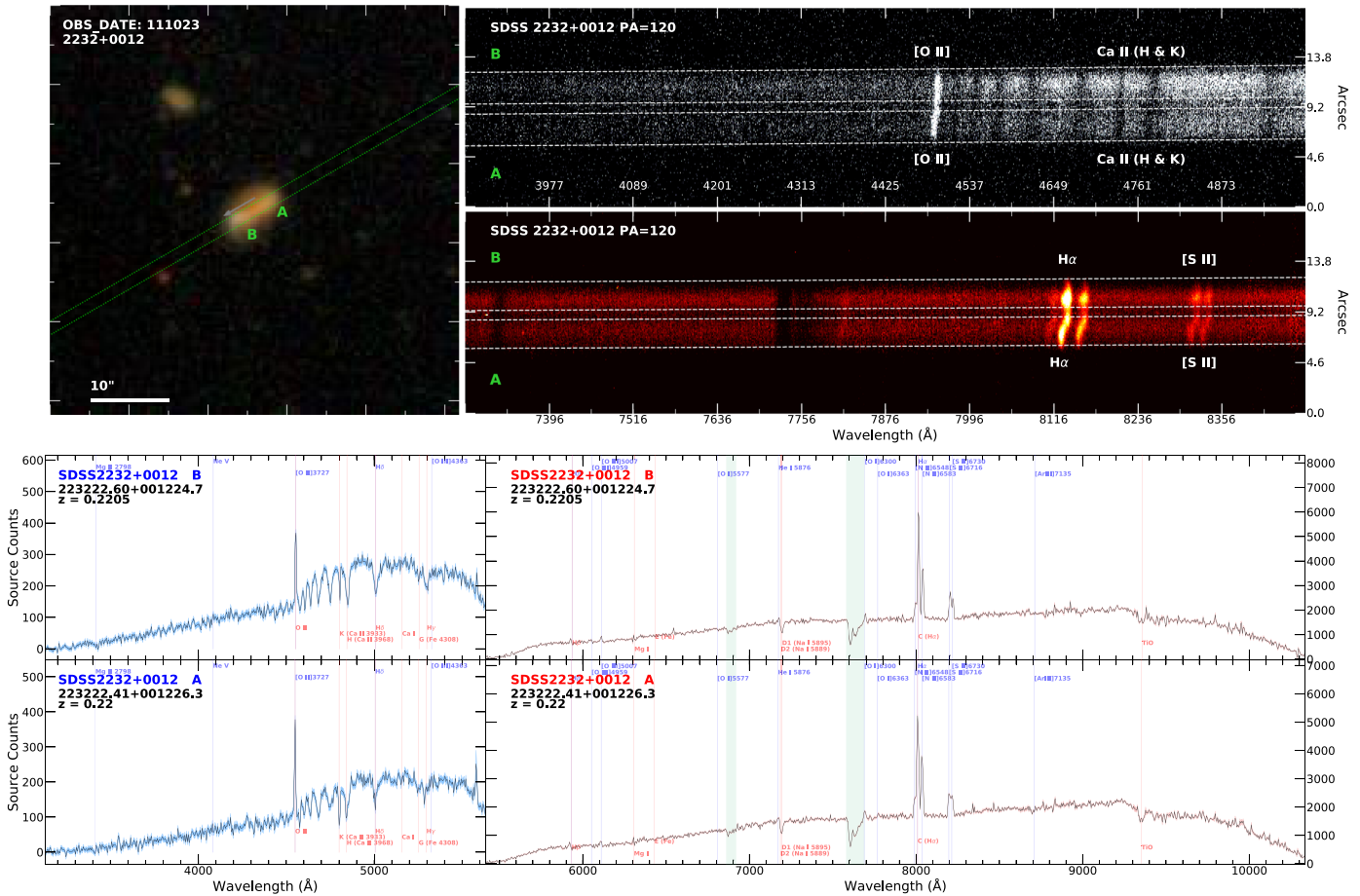
---

[6] https://www.nist.gov/pml/atomic-spectra-database

Figure 1. Example of optical spectra reduction and redshift estimate. We show: Top left: the optical image with sources labeled A and B. The slit is overlaid (dashed green lines) with the gray arrow indicating the orientation of the slit. The source designation (J200) is given in the legend. Top right: 2D optical spectra. LRIS acquires data separately for the blue (upper panel) and red regions of the spectrum (lower panel). Sources A and B are labeled as the lower and upper extracted regions, respectively. We show the extraction regions with dashed lines which follow the polynomial terms given by the trace. We also indicate useful *landmark* spectral features. The brightness is rescaled arbitrarily for readability. Bottom: the 1D spectra for each extracted source in the pair before flux calibration. Emission and absorption lines are indicated with blue and red vertical lines, respectively, to estimate redshift. Strong telluric bands are shown as green-shaded regions. At this point in the pipeline, the blue and red sides of the spectra are still separated. We show an example pair that is spectroscopically confirmed as a dual source. The complete set of 32 figures (not including the 3 targets from archival SDSS data) can be found in the online journal.

(The complete figure set (32 images) is available.)

2.2. Spectral Fitting

For the remainder of the analysis, we focus on the kinematic pair subsample. We use the IDL-based spectral fitting package SPFIT that we developed and introduced in Fu et al. (2018), which is now publicly available.[7] The program simultaneously fits the stellar continuum and emission lines of a spectrum. The spectrum is modeled as a superposition of common emission lines and a weighted sum of simple stellar populations (SSPs), and matched to the wavelength-dependent resolution of each target spectrum. The spectrum is corrected for foreground Galactic extinction (Cardelli et al. 1989) and de-redshifted to rest frame, thus our redshift estimates serve as necessary priors. The SSPs are convolved with the line-of-sight velocity distribution (LOSVD), which is parameterized as a series of Gauss–Hermite polynomials to the fourth order. We run the fitting using a 6th-degree polynomial multiplicative corrective term, which encapsulates the effects of reddening and template mismatches (fits run using a Calzetti et al. 2000 extinction law yielded similar results). The SSP templates used in the fitting

routine are drawn from the MIUSCAT library (Vazdekis et al. 2012), which encompasses a spectral range of 3465−9469 Å, sufficient for the de-redshifted wavelength ranges of most of our sample. To reduce the number of free parameters in the fit, we tie the kinematics of all emission lines. While various emission line species could exhibit different velocity offsets due to outflows from disk winds, ionization stratification, or absorption from intervening IGM, we find that nearly all of our spectra with measurable emission lines can be well fit with tied emission lines. Only one source (014203.24-000151.0) shows a slight offset of Hβ, which we do account for in our fitting.

The fit itself is conducted in several stages, using the Penalized PiXel-Fitting (pPXF) method of Cappellari & Emsellem (2004) to solve for the weights of the SSPs, while independently using the Levenberg–Marquardt nonlinear least-squares minimization in the MPFIT package to solve the Gauss–Hermite LOSVD (Markwardt 2009). To obtain a reliable fit result for the complex composite spectral model, we break the total fitting routine into a series of three simpler fitting routines, obtaining reasonable guess values for the stellar continuum and emission lines separately. We begin by masking out regions of

---

[7] https://github.com/fuhaiastro/spfit

Table 2
Properties of Kinematic Pairs

Optical ID J2000	Obs Date YY-MM-DD	Grade	$z_{\rm spec}$	z-flag	Instrum	Sep (″)	Sep (kpc)	ΔV (km s^{-1})	AGN Class
(1)	(2)	(3)	(4)	(5)	(6)	(7)	(8)	(9)	(10)
005113.93+002047.2	01-11-13	A	0.11257	⋯	SDSS	3.4	7.0	3.0	1C, 2AS, 3, 4S, 5
005114.11+002049.4	00-09-25	A	0.11258	⋯	SDSS	3.4	7.0	3.0	1C, 2AS, 3, 4S, 5
013412.78-010729.5	00-10-03	A	0.07893	⋯	SDSS	4.6	6.8	120.1	1L, 2R, 3, 4F
013412.84-010725.0	03-01-04	A	0.07849	⋯	SDSS	4.6	6.8	120.1	1C, 2R, 3
014203.08-000150.3	16-09-07	B	0.71470	M	LRIS	2.5	18.0	399.4	⋯
014203.24-000151.0	16-09-07	B	0.71242	⋯	LRIS	2.5	18.0	399.4	4F
014715.86-000819.5	15-10-16	A	0.47248	⋯	LRIS	2.4	14.1	1148.4	4F
014715.94-000817.4	15-10-16	A	0.46684	⋯	LRIS	2.4	14.1	1148.4	⋯
014928.39-001445.7	15-10-16	B	0.08924	⋯	LRIS	2.1	3.5	22.9	1S, 2S, 3
014928.41-001447.8	15-10-16	B	0.08932	F	LRIS	2.1	3.5	22.9	1S, 2S, 3
015253.79-001005.6	15-09-14	B	0.08208	⋯	LRIS	2.3	3.6	9.1	2R, 3, 4F
015253.92-001004.3	15-09-14	B	0.08205	⋯	LRIS	2.3	3.6	9.1	1L, 2R, 3
020301.40-003341.7	16-09-07	B	0.69562	F	LRIS	2.4	17.1	423.9	⋯
020301.43-003339.3	16-09-07	B	0.69803	F	LRIS	2.4	17.1	423.9	4S
021021.00-005124.2	15-09-14	A	0.29120	F	LRIS	3.2	14.0	329.5	2R, 3
021021.13-005126.7	15-09-14	A	0.29262	F	LRIS	3.2	14.0	329.5	1C, 2S, 3
220634.97+000327.6	03-09-21	A	0.04656	⋯	SDSS	4.6	4.2	40.9	1C, 2AS, 3, 4S
220635.08+000323.3	03-10-25	A	0.04642	⋯	SDSS	4.6	4.2	40.9	1L, 2AS, 3, 4S
221142.42+002731.2	16-09-07	B	0.73652	P	LRIS	3.1	22.6	32.4	5
221142.51+002728.5	16-09-07	B	0.73633	⋯	LRIS	3.1	22.6	32.4	5
222051.55+005815.5	11-10-23	B	0.31789	⋯	LRIS	2.6	12.0	159.0	1L, 2R, 3, 4F
222051.70+005816.7	11-10-23	B	0.31859	⋯	LRIS	2.6	12.0	159.0	2R, 3
222907.53-000411.1	16-09-07	B	0.59284	⋯	LRIS	3.6	23.9	775.0	4F
222907.77-000410.9	16-09-07	B	0.59696	M	LRIS	3.6	23.9	775.0	⋯
223222.41+001226.3	11-10-23	A	0.22043	⋯	LRIS	3.2	11.4	178.0	1C, 2AS, 3, 4S, 5
223222.60+001224.7	11-10-23	A	0.22115	⋯	LRIS	3.2	11.4	178.0	1C, 2AS, 3, 4S, 5
223546.28+000358.8	15-09-14	A	0.79060	F	LRIS	1.8	13.5	106.1	4F
223546.40+000358.7	15-09-14	A	0.78997	F	LRIS	1.8	13.5	106.1	⋯
224426.44+001051.3	15-10-16	B	0.68952	M	LRIS	2.6	18.5	239.2	4S
224426.61+001051.9	15-10-16	B	0.69087	M	LRIS	2.6	18.5	239.2	4S
224532.53+005857.9	16-09-07	B	0.64727	⋯	LRIS	3.1	21.4	153.5	5
224532.68+005855.8	16-09-07	B	0.64812	⋯	LRIS	3.1	21.4	153.5	5
225222.52+010658.0	11-10-23	D	0.07150	⋯	LRIS	3.2	4.4	72.6	1L, 2R, 3, 4F
225222.65+010700.6	11-10-23	D	0.07176	⋯	LRIS	3.2	4.4	72.6	1S, 2AS, 3, 4F
225817.73+003007.7	15-09-14	B	0.25546	⋯	LRIS	5.1	20.3	658.1	4S, 5
225817.97+003011.5	15-09-14	B	0.25822	⋯	LRIS	5.1	20.3	658.1	1S, 2S, 3, 5
230010.18-000531.7	11-10-23	A	0.17929	⋯	LRIS	2.5	7.6	30.6	1L, 2R, 3, 4F
230010.24-000534.0	11-10-23	A	0.17941	⋯	LRIS	2.5	7.6	30.6	3, 4S
230342.74-011712.7	16-09-07	A	0.56534	⋯	LRIS	2.7	17.5	262.3	4F
230342.91-011711.9	16-09-07	A	0.56671	⋯	LRIS	2.7	17.5	262.3	⋯
231953.31+003816.7	15-09-14	B	0.90435	F	LRIS	3.7	28.8	894.1	4S
231953.43+003813.4	15-09-14	B	0.89867	F	LRIS	3.7	28.8	894.1	4S

Note. Every two rows is a pair, and sources are sorted in ascending R.A. (1) J2000 coordinate of the optical source; (2) Observation date; (3) Grade of the dual candidate (Paper I); (4) Spectroscopic redshift; (5) Flag for the grade of the redshift estimate where less certain (M = moderate, F = fair, P = poor, as described in the text), no tag indicates secure estimate; (6) Instrument; (7) Angular separation in arcsec between the optical counterparts in each pair; (8) Projected separation in kiloparsec; (9) Radial velocity separation in kilometers per second; (10) AGN classification flag based on optical and radio properties: 1 = BPT [N II] class (A = AGN-Seyfert, L = LINER, C = Composite, S = Star forming), 2 = WHAN diagram class (AS = Strong AGN, AW = Weak AGN, S = Star-forming, R = Retired), 3 = Radio Excess, 4 = flat (F) or steep (S) radio spectrum in the 6 GHz. core where $\alpha > -0.5$ is flat spectrum, and 5 = MIR color excess (W1 −W2 > 0.5) encompassing the pair.

the spectrum around emission lines, and fit only the stellar continuum with SSPs. The best-fit continuum model is then subtracted out from the spectrum, leaving an emission line-only residual spectrum, which is then fit with Gauss–Hermite templates to obtain guess values for the tied emission lines model. The guess values for the stellar continuum and emission lines are then used in a final simultaneous and nonlinear fit of the full spectrum using MPFIT. In this multistep approach, the kinematics of the stellar populations and the gas producing emission lines need not be tied together.

We show an example of the spectral fitting for one of our sources in Figure 2, where the inset panels highlight three regions of the spectrum important for ionization diagnostics. For brevity, we show 10 representative spectra in Figure 3 from our full 70 object sample, highlighting the range of spectral shapes and varying amounts of coverage. Plots of the fitted spectra for the entire optical sample, as well as the FITS files of the reduced spectra themselves, are available in the online material. We also fit the three pairs of galaxies with spectra from SDSS to be consistent. We obtain refined values for the

Table 3
Properties of Spectroscopically Determined Projected Pairs

Optical ID J2000	Obs Date YY-MM-DD	Grade	$z_{\rm spec}$	z-flag	Sep ($''$)
(1)	(2)	(3)	(4)	(5)	(6)
011156.44−000015.1	15-10-16	A	1.8190	M	2.5
011156.52−000017.3	15-10-16	A	0.25162	M	2.5
011613.73+005807.3	17-10-15	B	1.05635	⋯	5.4
011613.77+005801.9	17-10-15	B	0.94381	⋯	5.4
012050.37−004656.6	16-09-07	B	0.83148	⋯	3.3
012050.55−004658.4	16-09-07	B	0.48169	M	3.3
013505.89+011911.5	15-09-14	B	0.78436	⋯	3.2
013505.88+011908.4	15-09-14	B	0.35691	⋯	3.2
014457.10−004216.6	15-09-14	B	0.65363	⋯	2.5
014457.17−004218.8	15-09-14	B	0.31933	⋯	2.5
221331.60+004834.6	16-09-07	B	0.81902	P	4.3
221331.87+004836.1	16-09-07	B	0.90726	F	4.3
221806.92+004515.9	16-09-07	B	1.10099	⋯	2.2
221806.98+004517.9	16-09-07	B	0.83747	⋯	2.2
224204.25+003029.4	17-05-31	A	0.76231	F	3.1
224204.45+003028.1	17-05-31	A	0.51001	⋯	3.1
225002.04+001131.9	16-09-07	B	0.98811	M	4.5
225002.10+001136.3	16-09-07	B	0.52993	P	4.5
230223.28−000301.2	11-10-23	B	0.31059	⋯	3.3
230223.46−000259.4	11-10-23	B	0.54499	⋯	3.3
230453.04−010946.6	17-06-23	A	0.74477	M	1.7
230453.13−010945.5	17-06-23	A	1.43502	M	1.7
230559.17+002409.0	15-09-14	A	0.55594	⋯	1.6
230559.19+002407.4	15-09-14	A	0.34530	⋯	1.6
230858.68+002527.8	16-09-07	A	0.94002	P	3.7
230858.75+002531.4	16-09-07	A	1.4150	⋯	3.7
231843.30+004527.2	11-10-23	B	0.27490	⋯	4.3
231843.55+004525.0	11-10-23	B	0.96101	⋯	4.3

Note. Every two rows is a pair, and sources are sorted in ascending R.A. All spectra obtained from Keck/LRIS. (1) J2000 coordinate of the optical source; (2) Observation date; (3) Grade of the dual candidate (Paper I); (4) Spectroscopic redshift; (5) Flag for the grade of the redshift estimate where less certain (M = moderate, F = fair, P = poor, as described in the text), no tag indicates secure estimate; (6) Angular separation in arcsec between the optical counterparts in each candidate pair.

redshifts of our targets through the spectral fitting routine (down to $z \pm 0.00001$), and we report the final spectroscopic redshifts for each source in the kinematic pair and projected pair subsamples in Tables 2 and 3, respectively. We note that two individual sources out of the 35 pairs could not be fit with SPFIT: 011156.44−000015.1 is at such a high redshift ($z = 1.8$) that there is no wavelength overlap with the SSP templates; 230858.75+002531.4 is a QSO with broad lines that cannot be properly modeled. Neither of these galaxies is within a kinematic pair, and so are not necessary to test for dAGN.

Because many of the parameters in the fitting are tied together, the formal errors calculated within MPFIT are often underestimations. The fractional error of the line flux ($\delta f/f$, the inverse S/N) is mostly driven by the amplitude-to-noise ratio (A/N) and the observed line width in pixels (intrinsic + instrumental dispersion). Using a suite of Monte Carlo simulations of Gaussian emission lines covering a range of these two parameters, we compute a two-dimensional polynomial describing $\delta f/f$. The best-fit width and A/N of the emission lines observed in the data are then used to compute their corresponding 1σ line flux error.

2.3. High-resolution Radio Imaging

We now focus on the radio emission of 17 of the 21 spectroscopically confirmed pairs in our candidate dAGN sample. The consistent redshifts of the components in these pairs confirm that they are at low projected separations and thus part of ongoing galactic mergers. However, high-resolution radio imaging is necessary to unambiguously confirm that each component in the pair contains a radio AGN. This would be evidenced by dual compact radio cores that are coincident with the galaxies' optical and infrared counterparts. At lower angular resolutions, one active core with radio jets/lobes aligned with and overlapping the companion galaxy may give the false impression of two cores. As we will show, the strategy employed in our sample preselection inadvertently leads to a large fraction of these jetted imposters, making high-resolution follow-up a necessity. The VLA at 6 GHz is well suited for measuring the spatial extent of these close pairs, with angular resolution of $\sim 0''3$.

As with the optical spectroscopy above, the radio observations were conducted over three campaigns, between 2015 and 2018. In addition to the six kinematic pairs discussed previously in the pilot study of Paper II, we have observed 11 more of the spectroscopically confirmed kinematic pairs above. Of these 11 new pairs, three are considered grade A candidates and seven are grade B candidates, where the loose grading categories were based on the goodness of alignment between their optical and 1.4 GHz radio counterparts (see Paper I). As noted above, we include J2252+0106 despite its lowered grade. We note that this total of 17 pairs observed does not include four of the kinematic pairs from Table 2, which were generally of poorer S/N in the optical (we discuss these four pairs further in Section 4.2). All observations were conducted using the VLA in the A configuration using the C-band receivers, where the 4 GHz total bandwidth has a central frequency at 5.9985 GHz. The first series of new observations was conducted in autumn of 2016, with targets grouped into two scheduling blocks of 2.6 hr. The remaining observations were taken during spring of 2018, with two scheduling blocks of 2.0–2.6 hr. The details of the observations are given in Table 4.

We utilize the Common Astronomical Software Applications (CASA) package v5.6 with VLA-specific procedures to perform data calibration and flagging to generate the measurement sets for each observation. We use the updated CASA routine `tclean` to perform synthesis imaging and deconvolution. The Briggs weighting scheme with a robust parameter of 0.0 achieves a balance between resolving small-scale structure (necessary for constraining AGN core emission) while preserving the image fidelity by not boosting the rms noise of the image too much. We note that we did try a variety of robustness settings, as well as the natural weighting scheme; however, this did not result in any additional detections significantly above the background in any of the images. The average restoring beam size has an FWHM of $0''43 \times 0''32$, with the specific values for each image given in Table 4. We choose a pixel scale of $0''05$ for the images such that $\leqslant 5$ pixels fit within the restoring beam. Cleaning is run iteratively until one of two criteria are met: either the residuals drop below a threshold of $\sim 12\,\mu{\rm Jy}\,{\rm beam}^{-1}$, or 5000 iterations are performed. As with the optical data, we reanalyze the sample of six 6 GHz VLA images from Paper II in a homogeneous fashion with the new observations, with the exception of
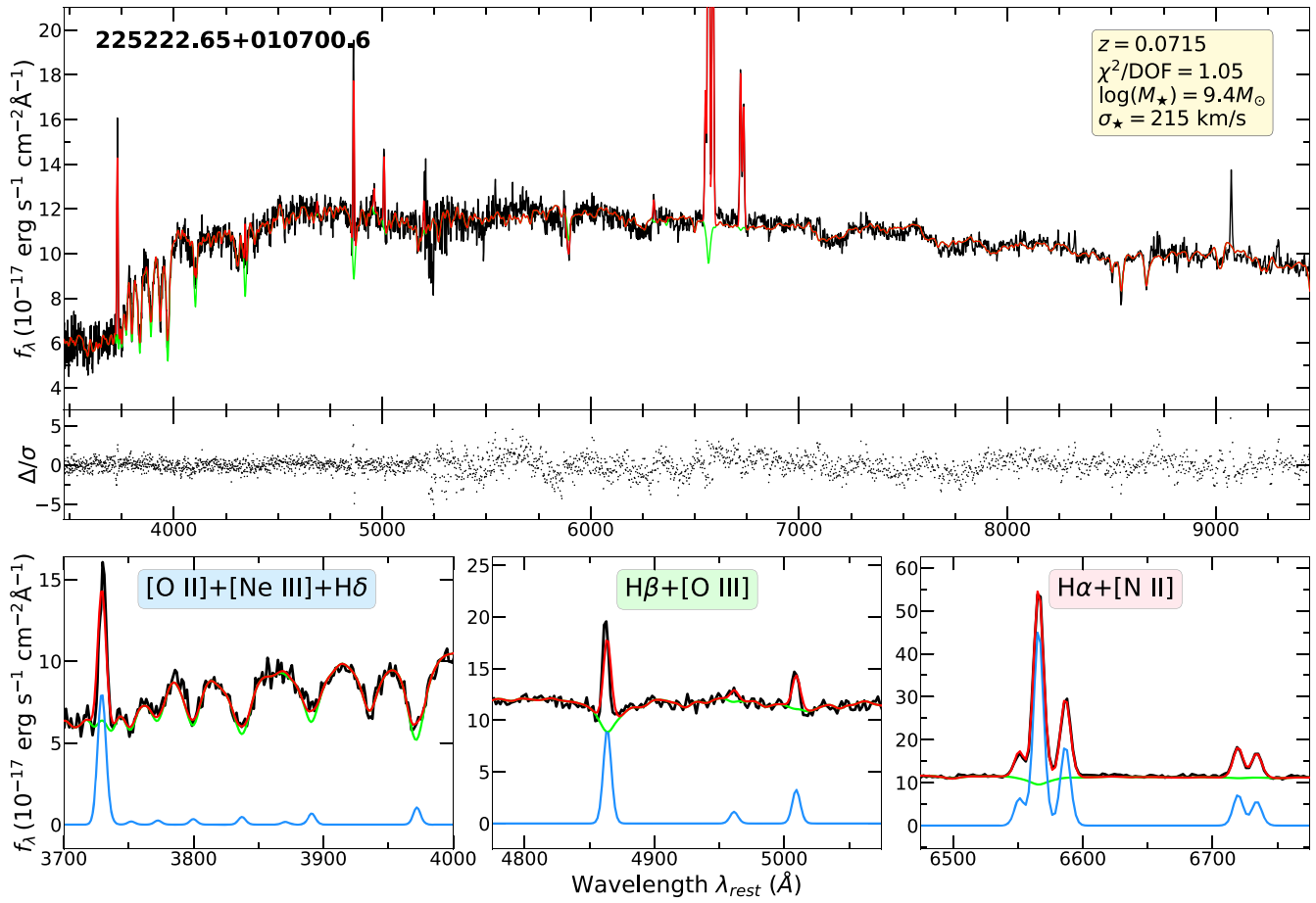
Figure 2. Example of the final fluxed spectrum for the source 225222.65+010700.6 from the kinematic pairs sample with the results of spectral fitting using SPFIT. The top panel shows the full region of the de-redshifted spectrum that is covered by the SSP templates. The lower subpanels show zoom-ins of important nebular emission line regions. The black line is the data (log re-binned), the underlying green line shows the best-fit stellar continuum model, the blue line gives the continuum-subtracted emission line model, and the red line is the total resulting best fit. We give some of the relevant output quantities in the inset box. The residuals (normalized by the error) are given in the lower portion of the top panel. Many of our spectra do not have wavelength coverage out to the Hα region after de-redshifting. In these cases, the subpanel is left empty. The complete set (70) of our spectral fitting plots is available in the online journal.

(The complete figure set (70 images) is available.)

J0134-0107 where we opt for the previous image which utilized a primary beam correction for a cleaner image. Using the multi-term multifrequency synthesis method, we model the spectral map of each image as a power law using two Taylor terms where the ratio of the first and zeroth terms then gives a map of the spectral index.

3. Analysis

Using the cleaned optical and radio data, we now investigate the properties of each kinematic pair to establish whether they contain dAGN. We begin by analyzing the optical emission lines with a battery of well-known diagnostic tests. We then analyze the spatial extents of the cores in the radio images to assess radio source presence and compactness.

3.1. Optical Emission Line Analysis

We use the optical line fluxes to diagnose the origin of ionization in each galaxy. The widely used BPT diagrams (Baldwin et al. 1981) use dust-insensitive ratios of strong optical emission lines to discriminate between two main sources of ionizing flux: (1) hot young populations of O and B stars from recent star formation; and (2) the ionizing

spectrum of an AGN. In Figure 4, we plot the two most commonly used BPT diagrams for the kinematic pairs that have detectable emission lines. However, we note that our diagnosis of optical AGN signatures given in Table 2 is based only on the [O III]/Hβ versus [N II]/Hα diagram. It is important to also note that the redshift range of the sample prevents us from obtaining emission line fluxes for much of the sample. For the entire set of 68 galaxies that could be fit, 39 galaxies are at high enough redshift ($z \gtrsim 0.47$) that the Hα complex is not covered, and 13 of these do not have coverage of the [O III] complex.

Out of the 42 galaxies in the kinematic pairs, only 17 have all four emission lines necessary for plotting on the BPT diagrams. We find that of these, four are classified as starburst galaxies, six are low ionization nuclear-emission regions (LINERs) by the criteria of Kewley et al. (2006), and seven are starburst/AGN composites that fall within the region bounded by the theoretical and empirical starburst relations of Kewley et al. (2001) and Kauffmann et al. (2003), respectively. We do not detect any Seyfert-type AGNs in our sample. It is not surprising that so many of our kinematic pairs fall in the composite region since the same ongoing merger effects which stimulate inflowing gas that fuels AGN likely also contribute to reinvigorated star formation. While we do not rely on the
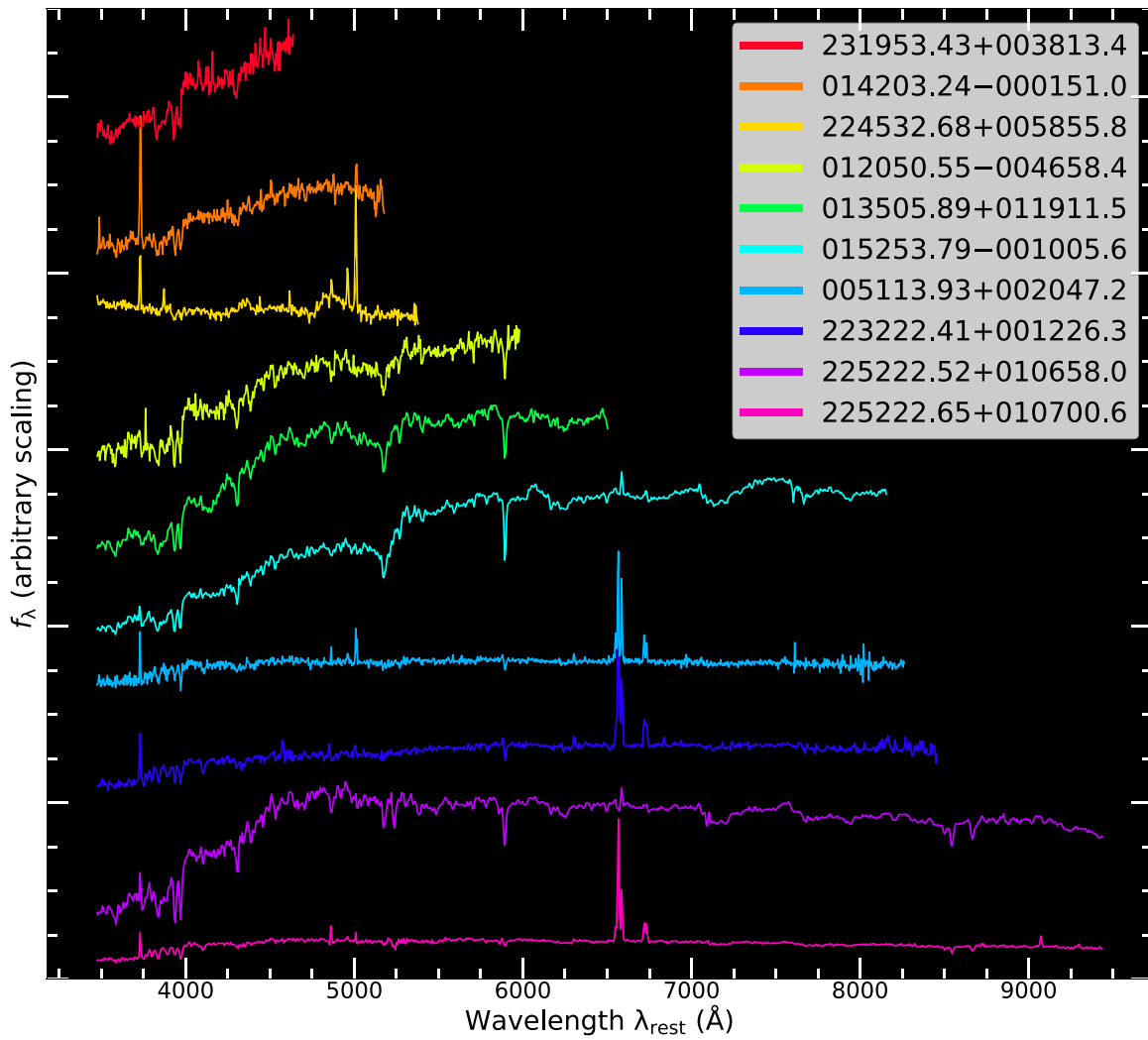
Figure 3. A sampling of the various optical spectra in our sample. The objects are ordered based on coverage within our spectral fitting routine, where the (de-redshifted) fitted range is heavily truncated at increasingly high redshift thus limiting which emission lines are within range. Fluxes have been rescaled for comparison. The full set of fitted spectra figures is available in the online journal. We also include the full set of simplified reduced spectra (including the subset shown here) as FITS files of the data behind the figure, formatted to be compatible with SPFIT.

(The data used to create this figure are available.)

[S II]/Hα classification for diagnosing AGN, we do note that the classifications are largely consistent with those found using [N II]/Hα. The most noticeable discrepancy is that one galaxy (014928.38-001446.0) moves from a classification as purely star forming to that of a Seyfert. For comparison, we show the full distribution of SDSS DR7 galaxies with optical emission line values from Thomas et al. (2013) as the grayscaled background.

The large share of LINERs in the kinematic pairs sample warrants closer inspection. Stellar populations of hot low-mass evolved stars ($t_{age} > 10^8$ yr) can produce emission line ratios similar to LINERS, making it difficult to separate weak AGN activity from so-called *retired* galaxies using only the BPT diagram. We therefore also classify our kinematic pairs using the Hα equivalent width (WHAN) diagram of Cid Fernandes et al. (2011) shown in Figure 4. Requiring measurements of only two emission lines, we note that we are able to classify three additional galaxies on the WHAN diagram; however, all three are classified as retired galaxies with Hα EW < 3 Å. The

majority (5/6) of the BPT LINERS are also reclassified as retired galaxies, whereas the majority (5/7) of BPT-composite galaxies fall above the threshold of strong AGN (EW > 6 Å). While we find no weak AGNs in our sample, one LINER does pass the criteria validating optical strong AGN classification. It is interesting that our radio-selected sample does not show any unambiguous optical emission line evidence of AGN activity.

We can further infer the presence of AGN based on the star formation rate (SFR) using the Hα luminosity. Assuming that the Hα luminosity encapsulates the total SFR, we can estimate the expected amount of radio power emitted by star formation. Many of our galaxies are star-forming, ambiguous composites, or LINERs in retired galaxies, implying that the observed optical ionization is not due to radiative/quasar mode AGN. We therefore check for excess radio power above what is expected from purely star-forming regions; significantly more radio power than the expected value cannot be explained by star formation alone, and could imply jet/radio mode AGN. We calculate the SFR using the prescription of Murphy et al. (2011):

Table 4
6 GHz Radio Properties of Sample

Radio Designation J2000 (1)	UT Date (2)	IT (minutes) (3)	Rms (μJy bm^{-1}) (4)	Beam (arcsec) (5)	P.A. (deg) (6)	$S_{6\,\mathrm{GHz}}^{\mathrm{tot}}$ (mJy) (7)	$\alpha_{4-8\,\mathrm{GHz}}$ (8)	Maj (arcsec) (9)	Min (arcsec) (10)	P.A. (deg) (11)
005114.11+002049.5	2015 Jul 6	60.0	4.8	0.28 × 0.26	+153.0	0.933 ± 0.011	−0.85 ± 0.02	0.206 ± 0.006	0.189 ± 0.005	+153 ± 18
005113.93+002047.2						0.297 ± 0.008	−0.96 ± 0.01	0.073 ± 0.024	0.038 ± 0.036	+39 ± 59
013412.78-010729.4	2015 Jul 6	20.8	22.7	0.32 × 0.25	−24.0	⩽10.017 ± 0.015	+0.27 ± 0.22	⩽0.316 ± 0.000	⩽0.250 ± 0.000	⩽+157 ± 0
014203.25-000150.8	2018 Mar 3	59.3	46.8	0.52 × 0.39	+36.6	⩽0.655 ± 0.008	−0.47 ± 0.13	⩽0.344 ± 0.003	⩽0.264 ± 0.002	⩽+20 ± 1
014715.86-000819.4	2016 Oct 4	59.1	13.4	0.37 × 0.30	+41.7	0.311 ± 0.007	−0.14 ± 0.03	0.067 ± 0.026	0.043 ± 0.029	+95 ± 50
015253.79-001005.5	2016 Oct 4	59.0	32.3	0.38 × 0.30	+44.5	⩽0.330 ± 0.003	+0.10 ± 0.06	⩽0.264 ± 0.001	⩽0.159 ± 0.000	⩽+63 ± 0
020301.43-003339.1	2018 Mar 3	59.5	19.3	0.51 × 0.39	+34.6	⩽0.330 ± 0.007	−1.01 ± 0.10	⩽0.325 ± 0.004	⩽0.240 ± 0.002	⩽+45 ± 1
220635.08+000323.2	2015 Jul 5	58.0	4.5	0.28 × 0.24	+22.0	0.588 ± 0.010	−0.84 ± 0.05	0.175 ± 0.009	0.112 ± 0.013	+111 ± 58
220634.98+000327.6						0.069 ± 0.013	−1.21 ± 0.73	0.314 ± 0.088	0.155 ± 0.145	+66 ± 31
222051.54+005815.5	2015 Jul 5	16.4	9.9	0.28 × 0.24	+13.0	1.107 ± 0.025	−0.01 ± 0.17	0.281 ± 0.010	0.165 ± 0.012	+75 ± 4
222907.55-000410.9	2018 Mar 6	31.2	60.7	0.46 × 0.35	−14.9	⩽0.719 ± 0.010	−0.15 ± 0.16	⩽0.291 ± 0.025	⩽0.284 ± 0.024	⩽+165 ± 14
223222.60+001224.7	2015 Jul 5	57.6	4.2	0.27 × 0.25	+17.7	0.244 ± 0.008	−1.13 ± 0.10	0.129 ± 0.019	0.044 ± 0.038	+103 ± 48
223222.44+001225.9						0.133 ± 0.011	−1.40 ± 0.28	0.245 ± 0.043	0.181 ± 0.044	+128 ± 32
223546.27+000358.8	2016 Nov 1	58.6	6.4	0.38 × 0.28	+34.4	0.140 ± 0.009	−0.23 ± 0.20	0.339 ± 0.033	0.039 ± 0.063	+84 ± 6
224426.45+001051.1	2016 Nov 1	58.1	8.1	0.38 × 0.28	+34.9	0.136 ± 0.019	−0.66 ± 0.59	0.512 ± 0.092	0.121 ± 0.071	+35 ± 5
224426.60+001052.3						0.089 ± 0.038	−2.49 ± 1.18	0.688 ± 0.362	0.519 ± 0.267	+120 ± 78
225222.35+0010659.9	2015 Jun 30	58.1	4.9	0.31 × 0.25	+34.4	⩽0.017 ± 0.007	+0.49 ± 2.96	⩽0.343 ± 0.097	⩽0.183 ± 0.026	⩽+52 ± 0
225222.65+0010700.7						⩽0.092 ± 0.009	−0.36 ± 0.46	⩽0.350 ± 0.024	⩽0.244 ± 0.012	⩽+14 ± 5
225817.74+003007.5	2016 Nov 6	57.9	26.0	0.40 × 0.28	+40.0	⩽0.735 ± 0.008	−0.85 ± 0.14	⩽0.364 ± 0.003	⩽0.294 ± 0.002	⩽+83 ± 1
230010.18-000531.6	2015 Jun 30	57.6	5.0	0.32 × 0.25	+35.8	⩽0.498 ± 0.009	−0.38 ± 0.07	⩽0.316 ± 0.003	⩽0.253 ± 0.002	⩽+120 ± 2
230010.24-000533.9						⩽0.063 ± 0.009	−1.19 ± 1.41	⩽0.344 ± 0.034	⩽0.254 ± 0.019	⩽+6 ± 10
230342.74-011712.7	2018 Mar 6	60.0	32.2	0.48 × 0.35	−23.8	0.632 ± 0.008	−0.05 ± 0.00	0.173 ± 0.008	0.053 ± 0.017	+4 ± 4
231953.31+003816.6	2016 Nov 4	58.6	23.8	0.39 × 0.27	+38.4	⩽0.594 ± 0.008	−0.74 ± 0.09	⩽0.315 ± 0.003	⩽0.279 ± 0.002	⩽+16 ± 3
231953.43+003813.4						0.143 ± 0.015	−0.99 ± 1.00	0.565 ± 0.071	0.214 ± 0.039	+22 ± 5

Note. Sources are sorted in ascending R.A. For observations where two cores are confirmed, the dual cores are listed together. (1) J2000 coordinate of the identified 6 GHz radio source core; (2) UT date of observation; (3) Integration time for the observation, encompassing the kinematic pair; (4) rms noise for the cleaned image; (5) Restoring beam size (maj × min axes); (6) Restoring beam position angle; (7) Total flux density at 6 GHz within the source extent in millijansky; (8) Flux-weighted spectral index within the 4 GHz bandwidth contained within the source region, where the error is the weighted standard deviation; (9)–(11) Beam-deconvolved source sizes (FWHMs in arcsec) and 1σ uncertainties along the major and minor axes and the position angle of the major axis (degrees east of north). In cases of unresolved point sources (denoted with ⩽), the values for Column 7 are for the un-deconvolved regions, and are given as upper limits. The error of the 6 GHz photometry does not include the 3% uncertainty in the VLA flux density scale (Perley & Butler 2013).
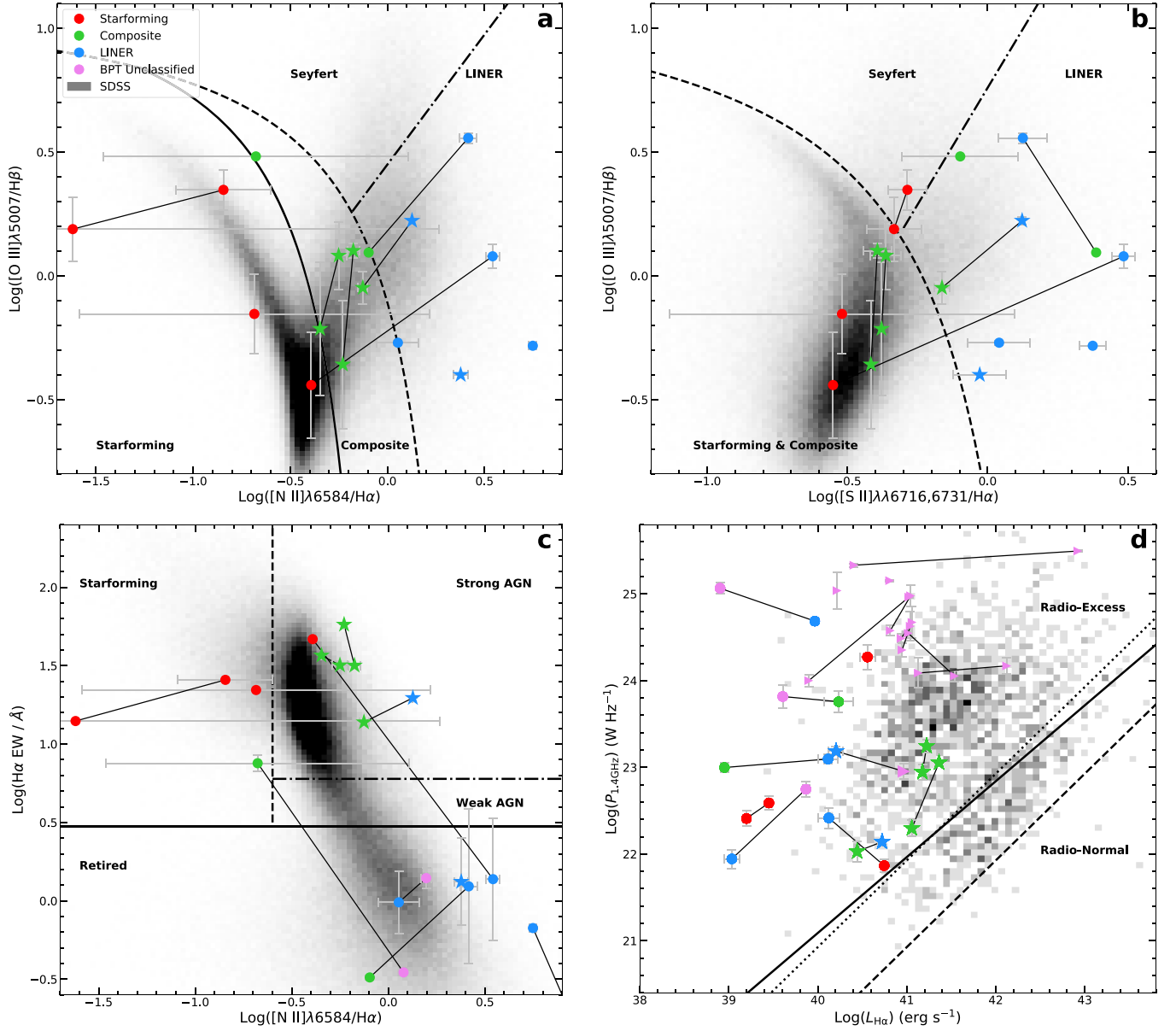
Figure 4. Optical emission line diagnostic plots for the kinematic pair subsample. (a). BPT plot using the [N II] emission line. Color coding for all four plots is taken from this plot, and described by the legend. The six pairs with dual radio cores are shown with stars, and the remainder of the kinematic pairs with circles. Lines connect pairs where both galaxies have sufficient information to be plotted. Pink points are objects that do not have information to be plotted in panel (a), but do have sufficient data to be plotted elsewhere. We maintain this same scheme in subsequent plots. The underlying grayscaled distribution is drawn from the SDSS DR8 sample of galaxies. Cases where error bars are large are usually due to low observed [N II] flux. (b) BPT plot using the [S II] emission line doublet. Notice that since some sources switch category from panel (a), the BPT diagrams cannot be trusted as the only metric for diagnosing AGN activity. (c) Hα equivalent width plot of Cid Fernandes et al. (2011), which is able to weed out objects with LINER signatures in the BPT plot where the signature is due to hot old low-mass evolved stellar populations. (d) Radio excess plot. The Hα luminosity is converted to an SFR via the relation of Murphy et al. (2011), and then translated to a predicted radio power emitted by that star-forming population. We plot sources with SFRs obtained via the Balmer decrement using triangles. The dashed line shows the one-to-one relation for the SFR between Hα and the 1.4 GHz radio power. The dotted line shows a radio power that is $10\times$ higher than that predicted for star formation. The solid line is the empirical relation given by Kauffmann & Heckman (2009) that splits the known bimodal distribution of radio galaxies, which is similar to the dotted relation. We find that all of the objects in the kinematic sample are above the solid line, implying a higher observed radio power than can be explained by star formation alone, suggestive of AGN activity.

$\log(\mathrm{SFR}/M_\odot\ \mathrm{yr}^{-1}) = \log(L_{\mathrm{H}\alpha}^{\mathrm{SF}}/\mathrm{erg\ s}^{-1}) - 41.3$. An analogous SFR prediction using IR luminosity can be used in conjunction with the empirical IR-radio correlation of star-forming galaxies to similarly estimate the expected radio power at 1.4 GHz (Yun et al. 2001; Murphy et al. 2011). We invert this to solve for the expected radio power using the Hα SFR: $\log(P_{1.4}^{\mathrm{SF}}\ (\mathrm{W\ Hz}^{-1})) = \log((\mathrm{SFR}_{\mathrm{H}\alpha}/M_\odot\ \mathrm{yr}^{-1})/(6.35 \times 10^{-22}))$. In cases where Hα is

not observable due to high redshift but Hβ is, we estimate the value of Hα via Hβ by assuming a Balmer decrement. We use a value of Hα/Hβ = 2.8 for case B recombination, appropriate for galaxies dominated by star formation (Osterbrock & Ferland 2006), since we are probing the SFR in our sample assuming the upper limit scenario where all Hα photons are resulting from star formation.

In panel (d) of Figure 4, we plot the distribution of observed 1.4 GHz radio power versus the Hα luminosity. The radio power is computed from the integrated flux densities from the VS82 survey and our spectroscopic redshifts. We plot the 21 galaxies in kinematic pairs that have detected or estimated Hα fluxes. Radio galaxies are known to follow a bimodal distribution of activity (Kauffmann & Heckman 2009), with a population of active radio galaxies exhibiting radio power more than $\sim 10\times$ the value expected from star formation. We show both this empirical relation and the theoretically expected relation computed above (Murphy et al. 2011), and note that all of the galaxies with detected Hα emission fall above these relations. For the LINERs especially, this implies that the radio power output by the galaxy is not coupled to the ionized gas optical emission from star-forming regions, suggesting the presence of AGN in addition to older stellar populations. We note that our computed values for $L_{H\alpha}$ are lower by ~ 0.5 dex than those presented in Paper I. This is partially because we did not perform a rigorous correction for slit aperture loss; however, several of those original values were overestimations based on the 3σ upper limits for undetected emission lines. Of the previously discussed sources, we note that only the galaxies in J0051+0020 and J2206+0003 were shown to be below the threshold given by Kauffmann & Heckman (2009), yet still well above the one-to-one SFR relation. As noted in Paper I, it is unsurprising that so much of the kinematic sample shows radio excess since within the full VS82 sample out to $z \sim 0.4$, the subset of *passive* galaxies without strong emission lines shows a strong preference (96%) to be radio excess.

3.2. 6 GHz Radio Emission Analysis

In Figure 5, we show the 6 GHz continuum and spectral index maps as well as a montage of archival imaging for the confirmed dAGNs, including the population of duals from Paper II. In each of these pairs, we see clear evidence of two separate compact radio cores more than 3σ above the rms noise of the background. We overlay contours from the 6 GHz images onto the deep SDSS optical co-added images and the UKIRT Infrared Deep Sky Survey (UKIDSS) near-IR (NIR) images to confirm that the radio cores are indeed well matched to the stellar nuclei. This is also consistent with the lower resolution 1.4 GHz radio contours. We find that one (J2319+0038) of the 11 new candidate pairs has convincing dual radio nuclei in the 6 GHz images that are coincident with their NIR and optical counterparts. There is also evidence of a secondary radio core in J2244+0010 that is not aligned with the remnant of jets from the companion AGN; we thus count this pair as a dAGN system as well. The obvious merger in J2252+0107 does contain at least one active AGN with a hotspot most likely due to a jet; however, the source in the western galaxy is so faint that it is difficult to constrain the presence of a radio core. Of 17 total spectroscopically confirmed candidate pairs with radio observations, only six are proven to be bona fide dAGN systems with separate radio cores.

In Figures 6 and 7 we show the remaining kinematic pairs. In these galaxies, we see a mixture of radio morphologies that indicate only one radio AGN per pair. The morphologies of these *imposters* fall into three categories: three are Fanaroff–Riley (FR) radio galaxies (Fanaroff & Riley 1974), with strong radio lobes impacting the companion galaxy creating hotspots that mimic a core coincident with the companion's stellar nucleus; four show clear evidence of a single compact core emitting a narrow radio jet; four exhibit only a single compact core with some sparse evidence of extended low-level jet activity. Unfortunately, it is impossible to weed out these imposters during candidate selection, which may appear as two separate nuclei either due to hotspots or extended diffuse emission within the $1''8$ resolution of the 1.4 GHz VS82 survey. This is an obvious limitation of the sample selection method, and should be anticipated in future medium-resolution radio surveys searching for small separation dAGNs. As a rough guide based on our results, similarly selected samples might contain as many as $\sim 53\%$ (9/17) jet-overlap imposters. Alternatively, our strategy could be effective for preselecting galaxy pairs to study jet interactions and termination shocks in clusters. We note that the confirmed dAGN in J2319+0038 does show a prominent jet in the northern core, but it is not aligned with the clearly detected separate core to the south and is thus unambiguously two separate structures.

In order to estimate the spatial properties of the radio cores of the confirmed dAGNs, we simultaneously fit two-dimensional elliptical Gaussians over each source in the cleaned Stokes *I* moment zero maps using the CASA task `imfit`. The best-fit Gaussians are then deconvolved from the restoring beam to give the intrinsic size and orientation of each source. In the case of J2319+0038NW, we apply a circular mask over the easterly extending jet to allow for component fitting. For cleaned images, the errors on a given pixel are correlated with those of the surrounding pixels, so errors are estimated within `imfit` using the prescription given by Condon (1997). The best-fit ellipses are then applied to the spectral index maps, allowing us to derive the flux-weighted spectral indices for each component. The resulting physical parameters of the dAGNs are given in Table 4. We analyze the imposters in the same way, confirming that only one compact source is detected per candidate pair. In cases with prominent jets, we only fit the region of the suspected core. For marginally resolved or unresolved point sources, `imfit` is unable to deconvolve the source from the beam. This most often occurs for sources with best-fit sizes smaller or equal to the beam size, where there are not one or two pixels clearly brighter than the rest in the region. For these cases, we give upper limit estimates of the integrated flux and spectral index based on the un-deconvolved fits.

The dAGNs are fairly compact, with spatial extents smaller than $\sim 0''5$, down to $\sim 0''07$. In most of the duals (10/12 individual sources), we see cores with steep spectral index values < -0.5, indicating regions of strong synchrotron emission. This may indicate that these AGNs have recently switched on, such that the jets have not had time to propagate outward. The single AGN systems with prominent jets consistently show flat spectrum cores, as would be expected for synchrotron self-absorption from an obscured nuclear region. We give details on each source and its final classification in the following section.

4. Discussion

Our sample of radio-selected dAGN candidates shows a variety of multiwavelength properties. In this section, we integrate the multiple lines of evidence to rigorously confirm our final sample dAGNs. We begin by highlighting each of the dual systems and explaining the criteria they satisfy to achieve dAGN status. We combine similar arguments for why each of the remaining systems in the kinematic pairs sample do not
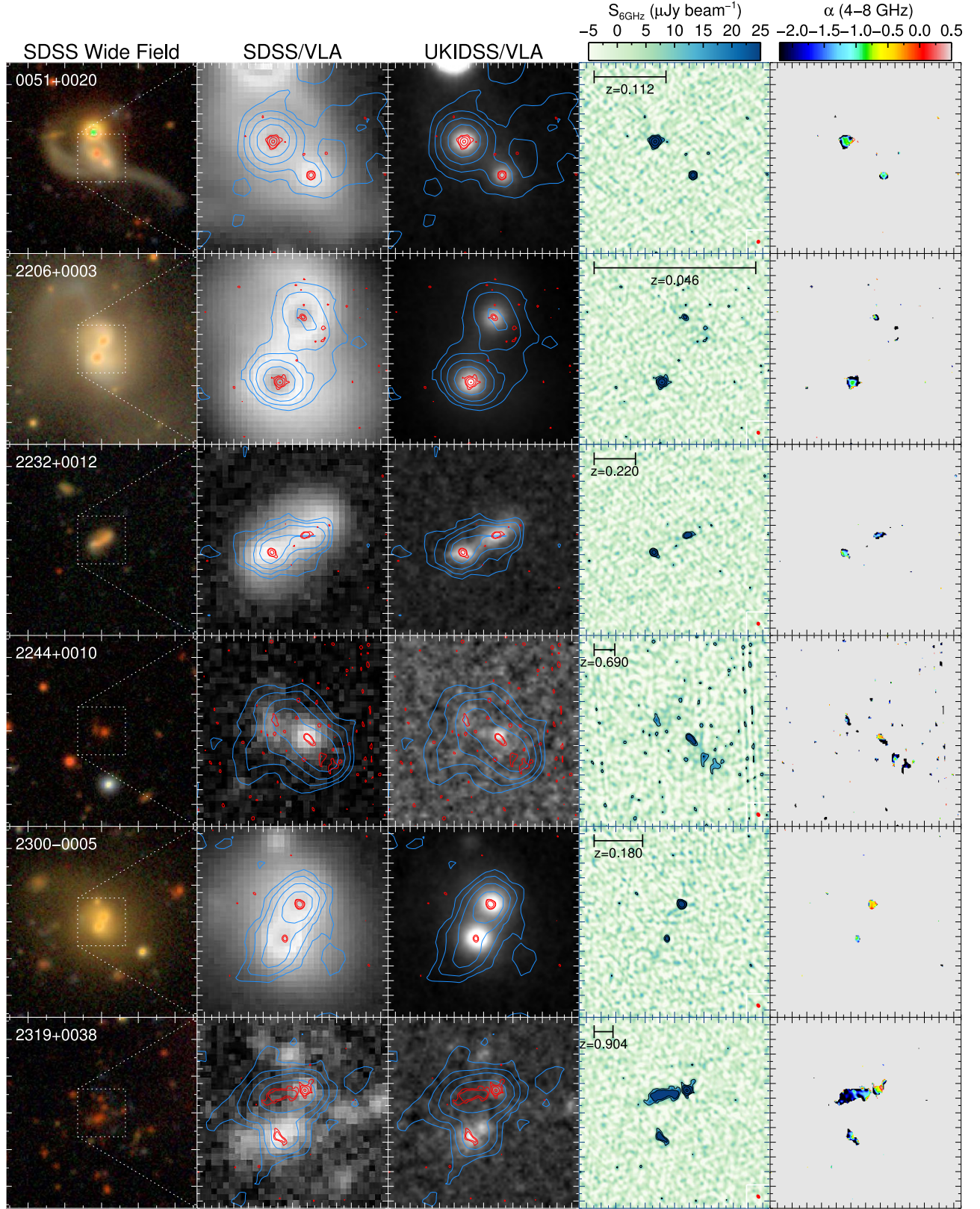
Figure 5. Montage of bona fide dAGN systems. Column (1) Wide-field deep SDSS Stripe 82 co-added optical images with source designation; (2) 4× zoom-in of the optical images (in grayscale for ease of viewing), with cyan contours from the VS82 1.4 GHz radio images and red contours from the 6 GHz VLA radio images; (3) archival UKIDSS NIR images with the same contours as in Column 2; (4) VLA 6 GHz radio Stokes I continuum map, with corresponding contours. Scale bars are 10 kpc; (5) 4–8 GHz spectral index map determined from the 6 GHz VLA data. In all cases, the lowest contour level is at 3σ, and the contours increase exponentially to the peak value. Major tick marks are spaced in $10''$ intervals in Column 1, and $1''$ intervals in all other panels. N is up and E is left in all panels.
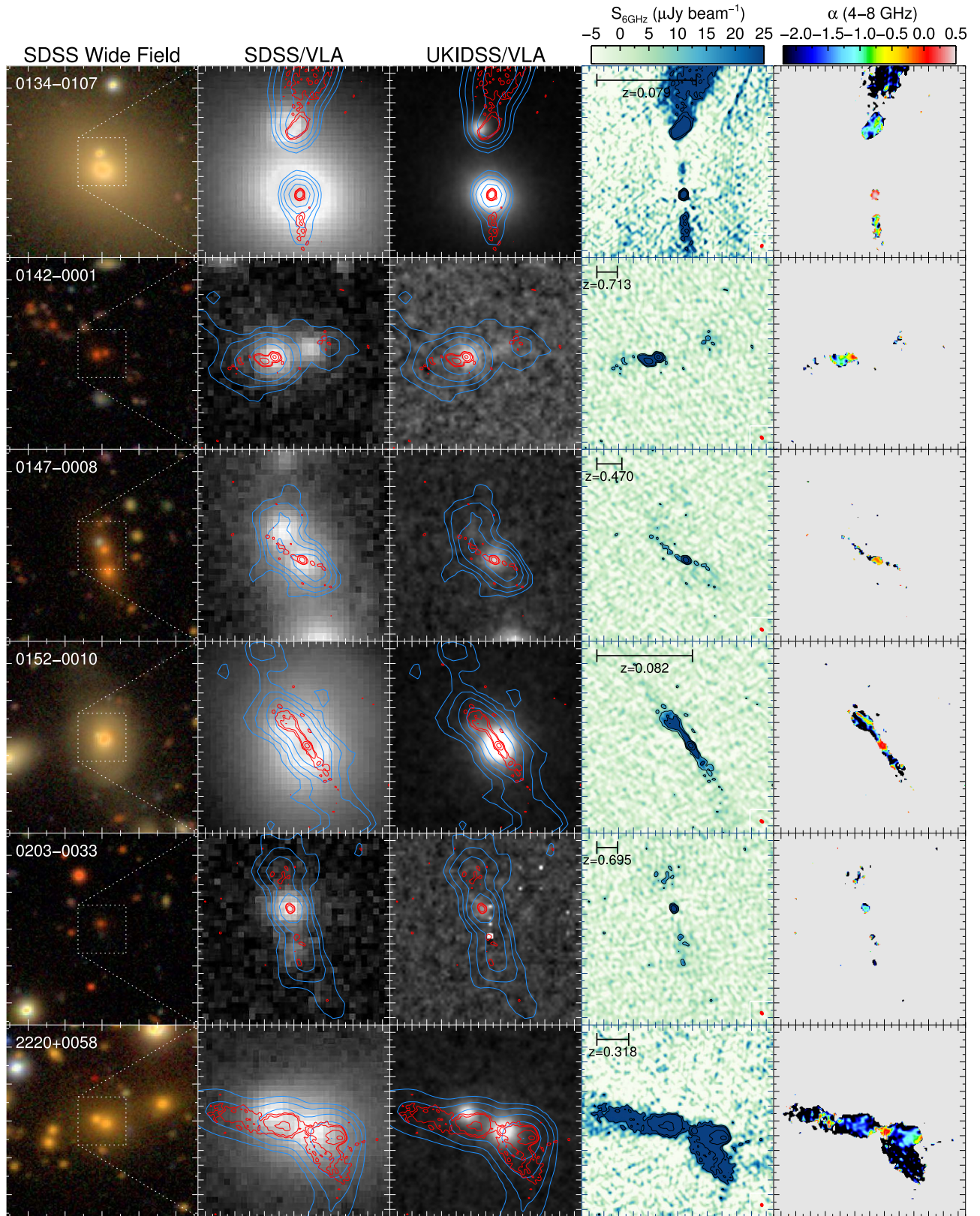
Figure 6. Same as Figure 5, but for single AGNs in kinematic pairs. Most of the galaxy pairs contain one AGN that exhibits obvious radio jets/lobes in the 6 GHz imaging, where varying amounts of the jets overlap with the companion galaxy, giving the false impression of two radio cores at lower resolution (blue contours).

qualify as a dAGN. We continue our discussion of the full kinematic sample by looking at the properties of the active nuclei and how they relate to their host galaxies. Finally, we finish with a discussion on the limitations of our sample

selection technique, and propose guidance for future surveys of dAGNs.

Our final census of dAGNs in the sample is guided by several criteria, shown schematically in Figure 8. We base our
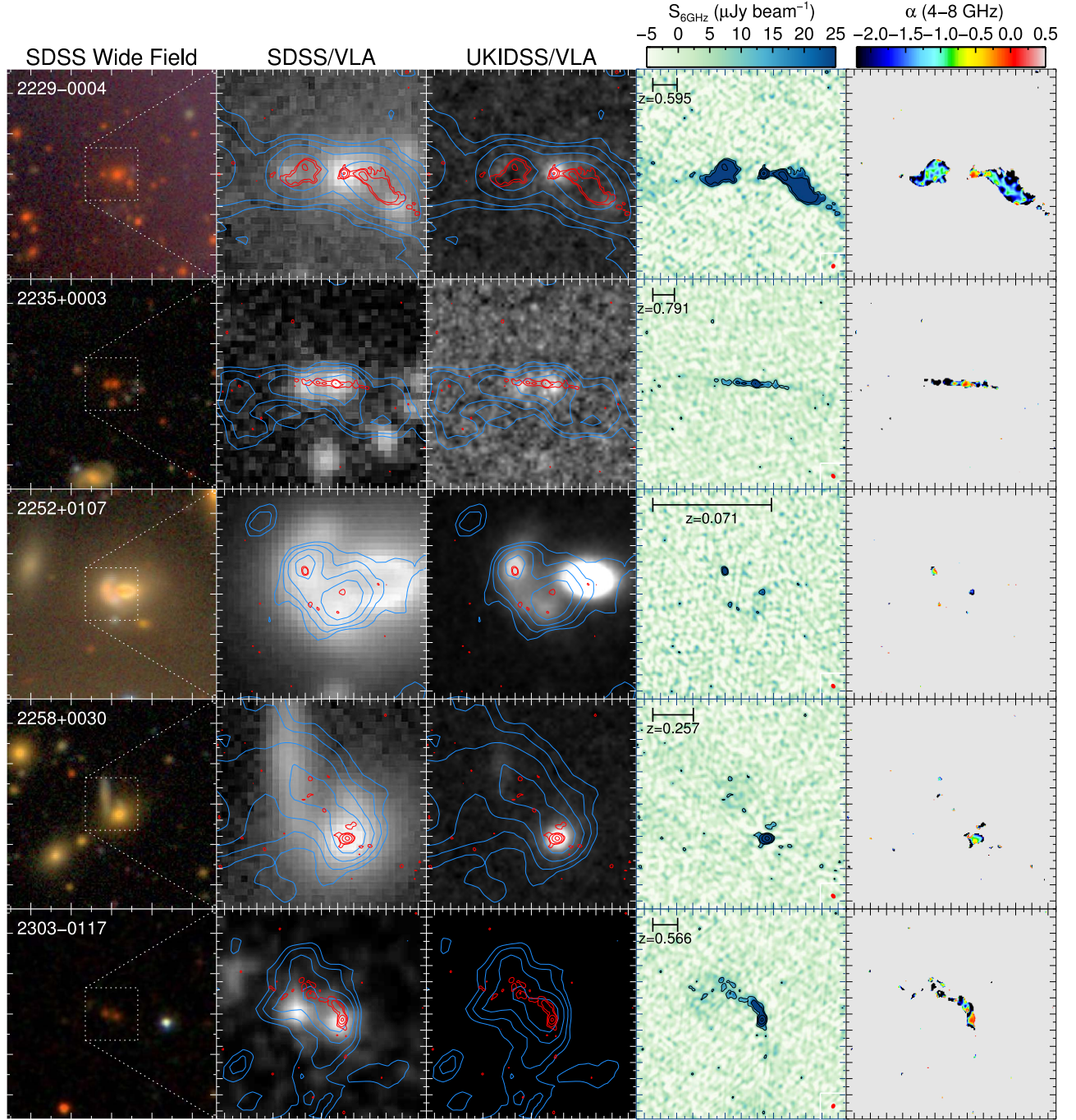
Figure 7. Continuation of Figure 6.

classification primarily on the 6 GHz radio imaging, where a dAGN system will exhibit two separate compact regions of high radio brightness above the background. As noted above, cases where one AGN is producing extended jets complicate this classification. For scenarios where a jet or radio lobe from one galactic nucleus overlaps with its companion, we consider optical emission line diagnostics of AGN activity in the companion to be strong alternative evidence for a dAGN system. In cases where overlapping jets are not an issue, we also consider the 1.4 GHz radio excess as a potential indicator of AGN activity. For several pairs in the kinematic sample without 6 GHz radio imaging, we rely on the optical properties and radio excess as signatures suggesting dAGN activity, but

do not consider these as robust confirmations compared to dual radio cores.

A widely used technique to preselect AGN involves making color cuts using mid-IR (MIR) magnitudes from the Wide-field Infrared Survey Explorer (WISE) mission (Wright et al. 2010). In Figure 9, we show the MIR colors from WISE for our kinematic pairs. Of the 21 kinematic pairs, 12 pairs have WISE coverage. The color selection criteria of Jarrett et al. (2011) constrains a region of the plot to reliably select dAGN in advanced mergers (sep < 10 kpc). However, Satyapal et al. (2017) note that this strict cut misses a substantial fraction of known dAGNs in the literature, and that a more relaxed cut of $W_1 - W_2 > 0.5$ captures ~2/3 of known dAGNs. Since ~66%
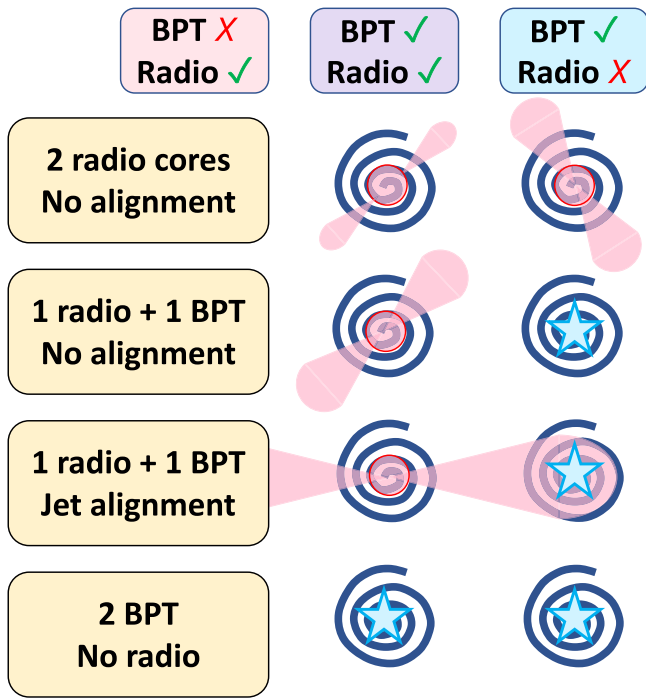
Figure 8. Four scenarios for dAGN classification in our sample. Some of the jetted imposters may have BPT optical AGN signatures, and thus constitute a dAGN system (third row). However, jetted imposter systems cannot be granted dAGN status based on the radio excess diagnostic since the provenance of the excess observed for a galaxy without a radio core is likely the companion galaxy from which the jets originate. We do not use the MIR color diagnostic as a means of verifying dAGN since the resolution of WISE encompasses both galaxies in a given pair such that the observed magnitude is actually a blend of both components.

of our kinematic pairs have separations >10 kpc, we adopt the less stringent cut from Satyapal et al. (2017) as an additional diagnostic for dAGN activity. The resolution of WISE ($\sim 6''$–$12''$) is larger than the angular separation of any of our kinematic pairs, therefore the WISE photometric magnitudes encompass both nuclei within a given pair. For the color cut above, both underlying host galaxies in a given pair would also be mostly covered by a single aperture for the majority of our sample. We thus plot the color of the combined dAGN system in Figure 9, and therefore cannot say definitively which of the galaxies (or whether both in a pair) satisfy the AGN color cut. We note that five of our dAGN systems are above the generous color cut, including the systems J0051+0020 and J2232 +0012. Intriguingly, the two systems that pass the more strict color cut (J2211+0027 and J2245+0058) are pairs for which we have no other diagnostic evidence of dAGN activity. We do note that these two systems show three of the four brightest $L_{[O\,III]}$ values out of the kinematic pair sample. Based on the observed line ratios, we can roughly infer that 3/4 of these galaxies are producing stars at a rate of $<2\,M_\odot\,\mathrm{yr}^{-1}$, so their high $L_{[O\,III]}$ might be attributed to narrow-line region activity. While we do not take this as definitive evidence of dAGN, it does highlight the breadth of galaxy pair properties in our radio-selected sample.

In the right panel of Figure 9, we plot the radio power versus the [O III] luminosity for the kinematic sample. As noted in Section 2.2 many of our galaxies are at redshifts high enough to exclude the possibility of measuring Hα; however, we do have [O III] measurements for most of the kinematic pair galaxies. We can thus gain some additional insight into the properties of

their host galaxies. As in the radio excess plot, radio galaxies have been found to follow a bimodal distribution. Galaxies with radio power above the empirical relation of Xu et al. (1999) are categorized as *radio loud*, which is similar to the definition based on the optical-to-radio luminosity ratio of Kellermann et al. (1989) as employed by Roy et al. (2021) where $R > 1$ is classified as *radio loud*. While this demarcation does not constrain AGN status, it does highlight the bifurcation in our sample. Most of the bona fide dAGNs lie on or below the demarcation, with optical emission suggesting either star-forming, composite, or LINER type using the BPT diagram. The copious optical emission of the composite galaxies and LINERs might be produced via retired stellar populations or perhaps quasar/radiative mode AGN. While we cannot rule out the possibility of retired stellar populations in many (pink points) of the radio-loud population, it is possible that their enhanced radio power is due to jet/radio mode AGN.

4.1. Bona Fide Radio dAGNs

We find that five of our kinematic pairs show clear evidence of dual compact radio cores. One additional pair (J2244+0107) shows tentative evidence of a second region of activity, yielding a total of six dAGNs.

Combining the optical line fluxes described in Section 3.1 with the radio properties, the individual AGN components can be classified as HERGs or LERGs based on the multistep system of Best & Heckman (2012). This classification is primarily based on the bimodal distribution in excitation index (EI ~ 0.95) of Buttiglione et al. (2010), but uses additional criteria for classification in cases where not all emission lines are observed. As done by Singha et al. (2021), we also classify based on the individual demarcations of Buttiglione et al. (2010) for [N II] and [S II] when [O I] is not available. We note the final classification in Table A3. We investigate whether both components in the confirmed duals are of the same class, or if there is a mix.

4.1.1. J0051+0020

This pair exhibits two well-defined small-scale radio cores coinciding with two BPT-composite nuclei. The WHAN diagram shows that the optical nuclei are likely due to strong AGN, which are also likely the source of the mechanical power driving the radio excess above the Hα-predicted levels. While we cannot resolve which nucleus in the pair is responsible for the WISE IR AGN signature, the detection of dAGN in both optical and radio suggests that perhaps both galaxies contribute to the classification. We also note that Paper III found this pair to have X-ray detections for both nuclei with luminosities in the low luminosity AGN regime ($\log(L_{2-10\,\mathrm{keV}}/\mathrm{erg\,s}^{-1}) = 41.49$ and 40.95 for the N and S nuclei, respectively). Taken together, these traits make this pair the most concretely identified dAGN in our sample. We also note that neither galaxy is classified as radio loud by the empirical relation of Xu et al. (1999) or the R parameter of Kellermann et al. (1989), suggesting that both nuclei are operating in radiative/quasar mode. However, both sources are classified as LERGs, implying that the observed cores are actually emitting unresolved small-scale jets in radio mode activity, consistent with the steep spectral index values for both sources and lower Eddington ratios.
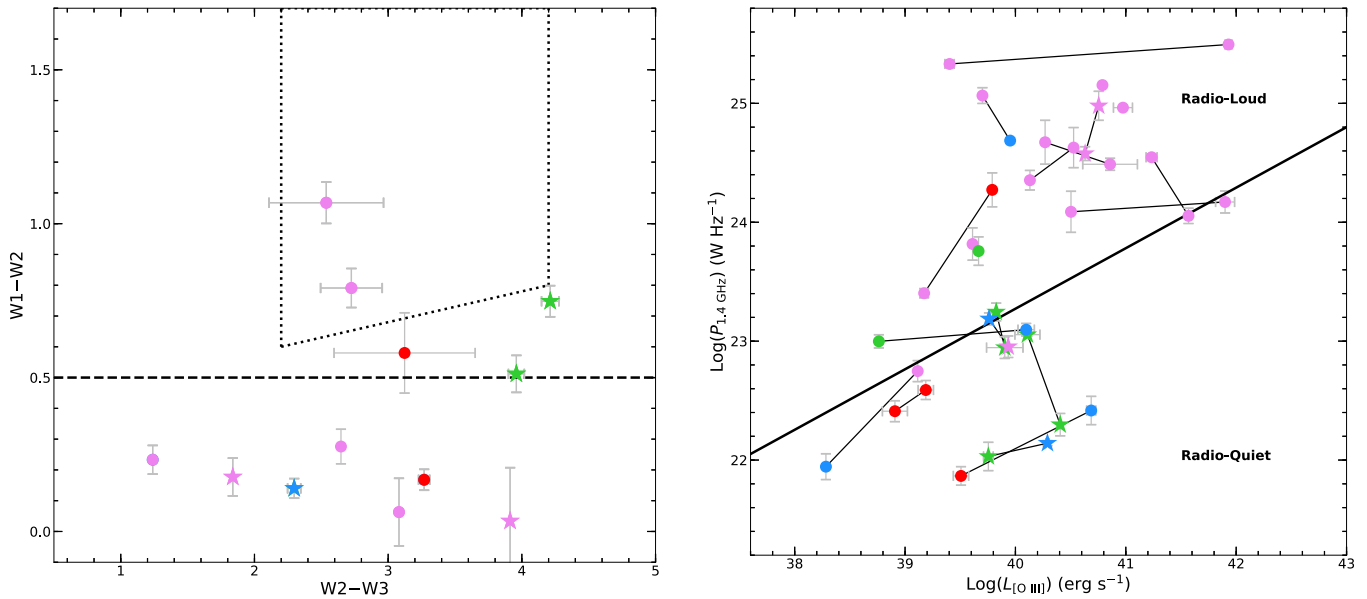
Figure 9. Left: WISE IR colors for the kinematic pairs. Note that the finest angular resolution of WISE ($\sim 6''$ for W1) is greater than the separation of any of our kinematic pairs. Thus, only one point is plotted for each pair and represents the composite color of the system. A total of five of our kinematic pairs have WISE colors that exceed the W1–W2 = 0.5 color cut from Satyapal et al. (2017), suggesting that at least one galaxy in the pair is exhibiting AGN activity. A more stringent cut for AGN is given by the box based on Jarrett et al. (2011), for which two of our pairs qualify. Note that these two pairs lack any AGN detections from the BPT diagnostics. Right: radio Loudness based on Roy et al. (2021) and Xu et al. (1999), comparing radio power against [O III] luminosity. As in the radio excess plot, the empirical demarcation is based on the known bimodal distribution of active galaxies. Galaxies above the relation are deemed radio loud and might be operating via the LERG mode of low accretion instead of the HERG/quasar mode.

4.1.2. J2206+0003

While both sources in this pair are well constrained to steep spectrum radio cores smaller than $\sim 0''3$ similar to those in J0051 +0020, we see differences between the optical nuclei in this pair. The NW galactic nucleus is an SF/AGN composite, while the SE nucleus is a LINER. Both are classified as strong AGN by the WHAN diagram, confirming that the nebular emission of at least the SE source is not due to old stellar populations. The radio excess in both components further implies the presence of dAGN. Neither source is found to be radio loud; however, both components are LERGs with modest levels of accretion and low X-ray luminosities ($\log(L_{2-10\ keV}/\mathrm{erg\ s}^{-1}) = 39.87$ and 41.99 for the N and S nuclei, respectively; see Paper III).

4.1.3. J2232+0012

This pair shows nearly identical evidence of dAGN activity as seen in the J0051+0020 pair. The system is classified as AGN by its WISE colors. Distinct from J0051+0020 is the classification of the SE nucleus as radio loud, while the NW component is radio quiet. The SE nucleus does appear slightly more spatially extended in the 1.4 GHz radio imaging implying more substantial jet activity, although extended jets are not seen in the higher resolution 6 GHz image, and only weak X-ray activity has been observed ($\log(L_{2-10\ keV}/\mathrm{erg\ s}^{-1}) < 41.51$ and <41.66 for the N and S nuclei, respectively; see Paper III). This might imply that we are seeing the beginning of the jet mode feedback as low-level accretion begins.

4.1.4. J2244+0107

At a substantial redshift (~ 0.7), [O III]/Hβ is the only emission line ratio detectable in the range of LRIS, making BPT or WHAN classification unattainable. We do note, however, that the SW nucleus is clearly coincident with a

steep spectrum radio core, and there is tentative evidence of an unresolved radio source coincident with the optical and IR images of the NE galaxy. The NE source does not appear to be well aligned with the radio lobe remnants to the SW of the companion galaxy. The spatial extent (~ 7.1 kpc) and flatness of the intensity distribution at 6 GHz suggest that a jetted AGN in the NE component cannot be ruled out at the resolution of our current observation. Two separate nuclei are further supported by the Hβ-propagated radio excess and radio loudness seen in both components. We note that the HERG classification of the NE nucleus is based on the [O III] EW due to the lack of observable emission lines, and thus should not be treated as conclusive; as well, there is significant uncertainty in the estimate of the higher accretion rate ($\log(\lambda) \sim -0.9$), although this would corroborate the HERG nature of the putative AGN in the NE galaxy.

4.1.5. J2300-0005

Only the NW galaxy exhibits detectable emission lines for classification as a LINER, though the WHAN diagram shows the nuclear ionization to be due to old stellar populations. Both nuclei do show radio excess beyond the levels expected for stellar populations. However, both sources have well-constrained compact radio cores. The flat spectral index of the NW core suggests synchrotron self-absorption of small-scale AGN jets by the galactic media. Both sources are tentatively classified as LERGs via [O III] EW, consistent with the observed low level of accretion and radio excess, as well as the low level of X-ray activity ($\log(L_{2-10\ keV}/\mathrm{erg\ s}^{-1}) = 41.35$ and 41.03 for the N and S nuclei, respectively; see Paper III).

4.1.6. J2319+0038

Interestingly, the high redshift of this pair prevents any optical classification, yet both sources exhibit steep spectrum

compact radio cores coincident with the optical and IR stellar nuclei. The unresolved point source in the NW galaxy is emitting a synchrotron jet that is not aligned with the companion nucleus. While we cannot classify either source as radio excess, we note that their high radio loudness ($R \geqslant 1.6$) is suggestive of radio mode accretion. At a separation of ~ 29 kpc, this system may have been triggered via tidal torques during its first pericenter passage, leading to the developed FR I morphology seen in the NW galaxy (Fanaroff & Riley 1974). The radio morphology of this pair is thus highly suggestive of two separate AGN; however, the wide separation precludes it from being categorized as a sub-kiloparsec dAGN. It could be that this system is in the earlier stage of galaxy pairing, and that both AGN were triggered by secular processes instead of merger effects. We therefore consider that this source presents a weaker argument for a dAGN system.

4.2. Other Evidence for dAGN Activity

The following kinematic pairs show a mix of optical evidence of AGN or radio excess. However, some of the spectroscopically determined kinematic pairs lack 6 GHz radio imaging follow-up due to redshift misidentification during our first pass of estimates. Therefore, we cannot say definitively if the observed radio excess in these pairs is from two separate sources or one with jets overlapping the companion. Additional radio observations could elucidate any putative cores.

4.2.1. J0149+0014

While this pair consists of two star-forming galaxies, both exhibit radio excess suggesting an additional source of radio power beyond star formation alone. We note that the NE blue disk galaxy exhibits Seyfert BPT line ratios in the [N II]/Hα and [O I]/Hα diagnostics, and is classified as a HERG by all selection criteria, suggesting that it may be transitioning to radiative/quasar mode activity.

4.2.2. J0210-0053

The NW galaxy shows only weak optical emission lines, likely due to older stellar populations. The optical signature of the SE galaxy is dominated by star formation. However, both galaxies exhibit radio excess, with good positional alignment between the 1.4 GHz radio images and the optical nuclei.

4.2.3. J2252+0106

This galaxy pair shows clear morphological evidence of tidal interactions due to an ongoing merger. The blue eastern galaxy is definitively classified as an ongoing starburst, perhaps prompted by the merger. The optically brighter yellow western galaxy is classified as a LINER by all BPT diagnostics; however, its nebular emission is shown to be due to retired stellar populations by the WHAN classification. Both galaxies show radio excess. This pair does have 6 GHz imaging, which shows a flat spectrum compact radio core coincident with each stellar nucleus. Both cores are barely detected and could not be deconvolved in our imaging analysis; thus, we cannot concretely designate this pair as dAGN. Interestingly, the eastern galaxy does show some faint evidence of a second radio detection, perhaps a relic from a previous radio jet that is not aligned with the western galaxy.

4.2.4. J2258+0030

This pair also has 6 GHz observations, clearly showing a compact steep spectrum core in the SW galaxy. While there are some scant hints of fragmented radio emission aligned between the two galaxies, there is no overlap with the NE galaxy. We cannot rule out that the radio excess observed for both components is not due to remnants of jets from the SW component; however, we note that the star-forming NE galaxy shows one of the highest degrees of radio excess (>2 dex) among the kinematic pair sample. Interestingly, this pair is one of the few that pass the WISE AGN color selection, although we cannot discern if this is due solely to the one well-detected radio core.

4.3. Single AGNs

In the remaining kinematic pairs, we discuss the evidence suggesting that one galaxy contains an AGN, and why we rule out the companion. In general, these pairs either show only one radio core, or are jetted imposters. After propagating the Hβ luminosities to estimate SFR, we note that J2229-0004NE and J2235+0003SE are the only galaxies in the remaining kinematic pairs to not exhibit radio excess, making high-resolution radio imaging crucial to avoiding misdiagnosing the origin of the radio power. Overall, these pairs serve as an interesting comparison against the duals, especially in the incidence of prominent jets.

The systems J0142-0001, J0147-0008, J2235+0003, and J2303-0117 all exhibit one flat spectrum compact radio core, but without any radio detection for the companion galaxies. None of the galaxies in these pairs exhibit optical evidence of AGN, although this is an artifact of their high redshifts ($z > 0.45$). Each pair shows evidence of fragmented jet structure originating from the active nucleus, with positional alignment with their companion galaxies that give the false impression of a secondary radio source at lower resolution. The seemingly one-sided jet in J2303-0117 appears to curve around, but not intersect with its companion galaxy, perhaps as a result of the orbital velocity as the galaxies make their first pericenter passage. In J0142-0001, there is a suspicious weakly detected clump of pixels $\sim 3\sigma$ above the noise in the vicinity of the NW galaxy, but it does not have a good degree of overlap with the stellar nucleus. We suspect that this weak signal is the back side of the luminous jet clearly seen protruding from the SE galaxy.

The pair in J0203-0033 is similar to the four jetted single AGNs discussed above, with the exception that the radio core in the NE galaxy shows a markedly steep spectral index, similar to those seen in the confirmed dAGN sample.

The galaxies in J2211+0027 and J2245+0058 do not have follow-up radio observations at 6 GHz, and their high redshift puts the diagnostic optical emission lines out of the observable range. However, these two pairs pass the WISE color selections of both Satyapal et al. (2017) and Jarrett et al. (2011), giving them the most convincing evidence of each harboring at least one IR AGN. High-resolution radio imaging might reveal dAGN in these systems. We note that the lower resolution 1.4 GHz observations suggest two separate radio cores in J2211+0027, while there is obvious evidence of a large-scale (>250 kpc) FR II jet aligned with the companion galaxy in J2245+0058.

As discussed in Paper II, only one galaxy in J0134-0107 is confirmed to have a radio core. While the northern galaxy does

exhibit a prominent radio hotspot coincident with the optical and IR nuclei, it is most likely due to an FR II lobe emanating from the southern source, in line with the southern-facing jet. Moreover, the northern hotspot is not spatially compact, and shows a spectral index similar to the southern jet. The optical properties of the sources do not conclusively suggest dAGN either. The northern galaxy is on the cusp of the composite-LINER division on the [N II] BPT diagram, and firmly within the LINER category on the [S II] diagram (the southern galaxy is definitively classified as a LINER); however, both are well below the $EW_{H\alpha}$ cut as retired galaxies, discounting AGN origin of their nebular ionization. We therefore rule out this pair as a dAGN

The remaining sources all show clear signs of well-evolved FR II radio lobes from one flat spectrum core that overlap the nuclear region of their companion galaxy. We therefore cannot argue that the observed radio excess for the companion is due to a potential AGN therein. The high redshift of the J2229-0004 system prevents any emission line analysis. The J2220+0058 system contains a LINER, but the WHAN designation of both galaxies as retired suggests against optical AGN classification. Similar evidence is seen for the J0152-0010 pair, although in this case the radio core and retired LINER nucleus are in different galaxies.

As is seen for these single AGNs in kinematic pairs, high redshift becomes a restriction not only on the availability of optical emission line information, but also on the spatial scale of prominent radio jets in the lower resolution images during sample selection. The former restriction introduces incompleteness into our sample: if we obtain NIR spectral coverage for the higher-z sources, say using the wide spectral coverage of the JWST NIRSpec instrument, then we could evaluate the entire sample using the BPT diagrams above (if they do show in fact show measurable emission lines). The latter complication is a direct consequence of our preselection strategy in Paper I where the requirement for two (often blended) radio detections can be also achieved by a single AGN jet with chance orientation in line with the companion galaxy. While evidently a major constituent of our sample, these jetted imposters are a necessary risk when employing a radio-based, and thus extinction-free, approach to finding dAGNs. On the other hand, recent discoveries of X-shaped radio galaxies, such as XRG J0725+5835, which hosts dual radio AGN at a nuclear separation of ~100 kpc, would likely be detected through our selection strategy (Yang et al. 2022). We suggest strategies to mitigate these challenges moving forward in Section 4.5.

4.4. Black Hole Accretion Rate and Duty Cycle of dAGN

With our final sample of AGN in kinematic pairs, we find conclusive evidence for dAGNs for 24% of the pairs based primarily on the radio morphology. If we include the tentative multiwavelength evidence for J2244+0107 and the pairs in Section 4.2, this fraction increases to nearly half the sample. We note that for the 17 pairs observed at 6 GHz, every single pair shows evidence of at least one radio AGN core. All of the confirmed dAGNs occur at separations below ~10 kpc except for J2319+0038, which is much more widely separated. The dAGNs are also consistently the most reliably classified as a composite of LINER types, though again, all but J2319+0038 are at $z < 0.2$. They are all hosted by massive galaxies ($9.0 < \log(M_\odot) < 12.0$), with modest SFR ($0.08 < SFR/M_\odot\ yr^{-1} < 1.26$), where H$\alpha$ is detectable. The SFRs propagated from Hβ (pink triangles in panel

(d) of Figure 4) extend beyond $>5\,M_\odot\ yr^{-1}$. This is not unexpected for galactic mergers; simulations predict that major mergers can centrally concentrate gas to instigate nuclear starbursts (e.g., Di Matteo et al. 2005; Hopkins et al. 2006, 2008). This effect has been observationally confirmed (Sanders et al. 1988), more recently with large samples from spatially resolved spectroscopic campaigns that reveal that star formation is indeed enhanced in the central-most regions of galaxies involved in major mergers (e.g., Ellison et al. 2008; Scudder et al. 2012; Steffen et al. 2021).

One of the most pressing outstanding questions in the field is whether galactic mergers instigate greater levels of black hole accretion via tidal torques. With our final subsamples of single and dAGNs in kinematic pairs, we address this question with some caveats. We begin by estimating the black hole mass for each galactic nucleus. In Paper II, we used the empirical relation of Kormendy & Ho (2013) between the black hole mass, $M_\bullet$, and the stellar velocity dispersion of the galactic bulge, $\sigma_\star$. However, the pilot study utilized primarily archival spectra from SDSS. Our final kinematic sample is composed of 86% of spectra from Keck LRIS, with a resolution that limits our measurements of the velocity dispersion to $\sigma_\star \gtrsim 200$ km s^{-1}. This limits our ability to reliably measure $\sigma_\star$ for ~25% of our galaxies in kinematic pairs. On the other hand, the estimate of the stellar mass for each galaxy is done by SPFIT using weighted sums of spectral templates matched to the spectral resolution, yielding a robust measurement of $M_\star$. We therefore choose to use the nearly flat stellar bulge mass relation of Kormendy & Ho (2013; intrinsic scatter of 0.29 dex):

$$\frac{M_\bullet}{10^9 M_\odot} = (0.49^{+0.06}_{-0.05})\left(\frac{M_{bulge}}{10^{11}M_\odot}\right)^{1.16\pm0.08}.$$

We estimate the bolometric luminosity of each galactic nucleus as the sum of the radiative luminosity from nebular emission and the jet mechanical power. From the 1.4 GHz radio luminosity, we compute the luminosity supplied by the AGN jets as $L_{mech} = 10^{43}$ erg s$^{-1}(L_{1.4\ GHz}/10^{24}$ W Hz$^{-1})^{0.7}$ (Cavagnolo et al. 2010). Provided that the galaxy has observable [O III] λ5007 emission, we can similarly estimate the radiative luminosity of the AGN: $L_{rad} = 3500L_{[O\ III]}$ (Heckman et al. 2004). We note that five galaxies in the kinematic pairs do not have observable [O III] emission, and thus cannot be used to infer a bolometric luminosity in this way. With the black hole mass estimates, the Eddington luminosity for pure hydrogen is $L_{Edd} = 1.26 \times 10^{38} M_\bullet/M_\odot$ erg s^{-1}. We calculate the Eddington-scaled black hole accretion rate as $\lambda_{Edd} = (L_{rad} + L_{mech})/L_{Edd}$.

We find the range of accretion rates for the dAGNs to be $-3.6 < \log(\lambda_{Edd}) < -0.9$, although all but one of these (J2244+0010 NE) have $\log(\lambda_{Edd}) < -2.0$. This implies low levels of accretion, as is common to jet mode LLAGN (Heckman & Best 2014). The single AGNs in kinematic pairs (ignoring those with misattributed radio power) run a similarly wide gamut of accretion rates ($-3.7 < \log(\lambda_{Edd}) < -0.9$), with considerably more scatter. The upper range of the singles is seen to approach ~10% of the Eddington limit, as expected for quasars, and indeed the majority of the HERGS are found to have values >-2.0. We see a similar distribution among the black holes in the projected pair sample, with a median value of $\log(\lambda_{Edd}) \sim -2.0$; however, without follow-up radio imaging of these pairs, it is impossible to say which sources are producing radio lobes that overlap their projected counterpart galaxies. At face value, our results suggest that there is no bias toward higher levels of accretion for dAGNs in mergers as compared to AGNs in isolated galaxies. This picture is not consistent with previous studies (e.g., Ricci et al. 2017, 2022,

and references therein), which have found a clear relationship between the accretion rate and the degree of obscuration. Namely, obscuration and activity increase with decreasing nuclear separation so that obscured AGNs dominate the fraction of AGN in mergers over LLAGN or unobscured AGN by a factor of at least 2 for separations comparable to those studied here (Koss et al. 2018). This persists until the effective Eddington rate is reached, triggering a blow-out phase that sweeps away obscuring material, leaving behind unobscured nuclei for some brief period of time. We attribute the accretion rate inconsistency found here to the high dispersions of the relations employed in estimating the Eddington ratios in our sample, as well as the bias toward unobscured AGN via optical spectroscopy requirements and lack of IR spectroscopy. More secure estimates of the black hole masses would be possible using reverberation mapping-based relations, although this is only practical for Type I AGN. Interestingly, it is now thought that there is a population of intrinsically (unobscured) Type II AGN at lower luminosities that might lack a broad-line region (Hickox & Alexander 2018, and references therein), which might partially explain the prevalence of Type II low accretion sources in our sample.

We do note that the four dAGNs observed in X-ray by Paper III showed that the low L_X range found for all sources classified them as either Seyferts or LLAGN. Characterization of the hardness ratios of the sample further excluded the possibility that the AGNs were heavily obscured; the low observed column densities suggested that the low level of luminosity, and therefore accretion rate, were intrinsic to the AGN. The remainder of our kinematic pair sample lacks archival Chandra observations; however, while we cannot effectively estimate the column densities, we can estimate the expected X-ray luminosities based on the black hole fundamental plane of activity of Merloni et al. (2005). The fundamental plane of activity is calibrated using isolated AGN, so our application of it here to dual systems is only done as a rough guide. In particular, we find that the SMBHs in our two new dAGNs would be expected to have luminosities in the quasar regime ($\log(L_X) > 44$ erg s^{-1}), although this is likely an overestimation since it has been shown that there are likely separate fundamental plane relations for radio-loud and radio-quiet populations (Bariuan et al. 2022). At these X-ray luminosities, it is expected that roughly 60% of AGN should be optically unobscured Type I AGN (Merloni et al. 2014), although clearly the dAGNs found in our sample do not fall into this category.

In discussing the duty cycle of *synchronized* black hole accretion, it is important to keep in mind that multiple AGN triggering mechanisms are at play. It is assumed that AGN in isolated galaxies accrete via stochastic processes in the absence of tidal torques from an ensuing merger. Stochastic accretion at a level given by the Eddington ratio of $\log(\lambda_{Edd}) \sim -3.9$ results in an estimated ~1% duty cycle for isolated AGN at $z < 0.5$ (Shankar et al. 2008). The rate of both SMBHs in a pair of merging galaxies that are synchronously accreting stochastically is then 0.01%. In contrast, merger-induced effects might also facilitate the building of the central gas reservoir necessary to activate an SMBH. However, this need not necessarily lead to synchronized black hole accretion wherein the chance of one galaxy being activated is intrinsically linked to the fate of the companion galaxy. This latter scenario is encapsulated in the correlated AGN fraction, ξ (Fu et al. 2018; Steffen et al. 2023),

which converts single AGN in pairs to dAGN due to correlated activities, including AGN cross-ionization between closely separated galaxies. This fraction is zero in the event of random pairing (i.e., chance simultaneous stochastic accretion in both galaxies in a pair). Both correlated and merger-induced effects can influence the dAGN duty cycle.

To evaluate the duty cycle of dAGN, we construct number densities for the 92 deg^2 of the Stripe 82 region, accounting for sample biases. If we conservatively focus only on the pairs with 6 GHz radio imaging as being rigorously confirmed, then we find a dAGN identification success rate of 29% (6/21) for our selection strategy of mergers selected via radio and optical imaging with follow-up optical spectroscopy. However, only 17 of these pairs had follow-up radio observations, so a corrected total number of dAGNs expected would be $N_{dAGN} \sim 7$ pairs ($=(6/17) \times 21$). The redshift range of the dAGNs inhabits a comoving volume of 2.665×10^8 Mpc^3, yielding $n_{dAGN} = 2.627 \times 10^{-8}$ Mpc^{-3}. We can obtain a rough estimate for the number density of galaxy pairs based on the galaxy stellar mass function of Baldry et al. (2012) Equation (6). This distribution is drawn from the Galaxy and Mass Assembly (GAMA)-II survey region, which covers roughly twice the area of the VS82 region with a high degree (98%) of spectroscopic completeness. We integrate across the stellar mass range of our dAGN sample to obtain $n_{gal} = \int \phi_{\mathcal{M}} d\mathcal{M} = 4.66 \times 10^{-3}$ Mpc^{-3}. We can then estimate the number density of galaxy pairs as $n_{pairs} = n_{gal} \times \gamma_m$. Here, γ_m is the redshift-dependent pair fraction for major mergers in close pairs from Robotham et al. (2014), as derived from the GAMA-II sample and archival samples assuming scaled nuclear separations of 20 h^{-1} kpc and velocity separations of 500 km s^{-1}. Our sample is restricted by design to select galaxy pairs in a well-defined range of close separations that are roughly equivalent to the scaling used in deriving γ_m, allowing for a reasonable comparison. For the mean redshift of our dAGNs ($z_{mean} \sim 0.36$), we obtain $\gamma_m = 0.034$, yielding $n_{pairs} = 1.57 \times 10^{-4}$ Mpc^{-3}.

The fraction of dAGNs within the comoving volume of VS82 can then be framed as $f_d = n_{dAGN}/n_{pairs}$. For the redshift range for our sample of dAGNs, we find $f_d = 1.7 \times 10^{-4}$. There are several caveats to this calculation that likely cause it to be an underestimation. The galaxy stellar mass function is known to evolve over time as mass is built up in galaxies at lower redshift (Ilbert et al. 2010). For the stellar mass and redshift ranges of our sample of dAGNs, this likely means that we have overestimated n_{gal}. While we corrected N_{dAGN} for incompleteness of radio observations, as noted above, the number still suffers from incompleteness at high redshift where emission line classification is not possible (although we note that in our sample we did not uncover any unambiguous optical emission line-selected dAGNs that were not also confirmed via radio imaging). There is also the bias to consider due to the incompleteness of our sample acquisition, such that the optically faint targets excluded from Keck follow-up might also contribute to f_d. Assuming a similar success rate of pair identification and dAGN detection as a rough estimate, we might expect the 18 unobserved candidates might contribute an additional 11 kinematic pairs, yielding approximately four additional dAGN systems, which would increase the fraction to $f_d \sim 0.03\%$. Of course, these fainter targets might be even more optically obscured than the main sample. For lower accretion rate sources, the fraction of obscured AGN ranges from ~40% to 80% (Ricci et al. 2017, 2021, 2022; Laloux et al. 2022), so the dAGN fraction is likely closer to $0.04\% < f_d < 0.13\%$ if we

correct for sources missed due to obscuration. Our cursory estimate of the dAGN duty cycle of $\sim0.02\%$ for optical/radio dAGN is thus a strict lower limit; however, it is still higher than the 0.01% expected rate for purely stochastic fueling of optical dAGN (Shankar et al. 2008). While it has been suggested that optical and radio AGN manifestations are distinctly different phenomena linked to different accretion states, the mean stellar mass of our dAGNs ($\log(M_{\mathrm{mean}}/M_{\odot}) \sim10.78$) corresponds to a similar stochastic dAGN duty cycle for radio activity of 0.01% (Shabala et al. 2008). We therefore conclude that the act of galactic mergers does play some role in funneling gas toward the inner nuclei of both galaxies to trigger synchronized activity.

The phenomenological models of Weigel et al. (2018) suggest a greater role of mergers in triggering AGN, such that major mergers are more likely to host AGN by as much as a factor of 10 over isolated galaxies. A similar factor of merger influence was found observationally by Goulding et al. (2018) using IR-selected AGN in a similar redshift range to our sample. Also, a recent study of galaxy pairs in the SDSS MaNGA survey by Steffen et al. (2023) finds that the rate of AGN in galaxy pairs is $2.5\times$ higher (and $40\times$ higher for dAGN) than what would be expected from random pairing, with a strong dependence on galaxy separation below 20 kpc suggesting important roles of both merger-induced and stochastic fueling processes in dAGN. Simulations of mergers paint a similar picture qualitatively. Hydrodynamical simulations predict that a major merger at separations <10 kpc ($\sim1/3$ of our kinematic pairs) can be observed as a dAGN $\sim16\%$ of the time (Wassenhove et al. 2012). Cosmological simulations based on Horizon-AGN have also suggested that most dAGNs found at separations < 30 kpc can be linked to ensuing galaxy mergers (Volonteri et al. 2022). We note that our dAGN fraction here is also lower than the value found using the pilot sample in Paper II, which focused on the most promising candidate dAGNs at much shallower comoving volume ($z < 0.2$). We attribute the discrepancy to the factors mentioned above, and offer some suggestions for mitigating strategies in the following section.

4.5. Prospects for Future Surveys

Based on the results above, we now offer some recommendations for how future samples of dAGN might be selected out of large surveys. As mentioned above, in selecting which sources from our parent sample would be observed to obtain optical spectroscopy, we employed a magnitude cut of $r < 23.4$ AB. This was done to ensure that observations of faint sources could achieve a minimum $S/N_{\mathrm{cont}} \geqslant 3$ during a maximum observation time of 60 minutes. While this magnitude cut is motivated by feasibility concerns, it also helps to select brighter galaxies that might be nearer to the universe. Closer proximity is desirable because at higher redshifts the signatures of radio hotspots from lobes and jets are less resolved and thus more easily confused with actual galactic cores, leading to a higher rate of projected pairs being observed in the initial sample selection phase. As we found in Section 2.1, our sample shows a wide range of redshifts, which is linked to their apparent optical magnitudes.

We illustrate the redshift distribution for the sample in the left and middle panels of Figure 10. In this case, we show the full sample from the optical spectroscopy including the projected pairs. The sample shows a wide range of $g - r$ and

$r - i$ colors, and r-band apparent magnitudes. In an effort to devise improved preselection criteria for future wide-area surveys, we investigate the apparent magnitudes from the SDSS photometric bands (without K corrections), assuming that we would not know the redshifts a priori. At a glance, lower redshift ($z < 0.5$) pairs are unsurprisingly found at lower magnitudes. Low-z pairs also appear to cluster blueward of $r - i \sim 1.0$. This is true for three of the four dAGNs in that redshift range. There is a much larger spread in the $g - r$ color dimension. This is consistent with the distribution seen in the full parent sample from the VS82 radio and optical cross-matched catalog, shown as the underlying gray points.

We investigate the redshift evolution of galaxy colors to illuminate possible trends using known spectral energy distributions (SEDs). We use the template spectra of Ilbert et al. (2008) and Salvato et al. (2008), which are a subset of the library from Polletta et al. (2007) of XMM Newton SEDs of sources in the COSMOS field. These templates cover a wide wavelength range from UV to IR for a full suite of galaxy types including QSOs. We highlight several diagnostic SEDs that have the most extreme changes in slope for a given type: elliptical, starburst, and QSO. We smooth the templates to a resolution of 200 Å as an ad hoc correction to account for the ~1000 Å width of the photometric bands. We then compute the colors for each smoothed SED at redshift intervals of 0.1. The resulting trends are shown in the right panel of Figure 10.

It is well known that QSOs occupy bluer color spaces than elliptical and starburst galaxies. The QSO colors in the right panel do not change much as a function of redshift, tending toward a locus of $g - r \sim 0.0$ and $r - i \sim 0.2$. The elliptical galaxies show a more dramatic redshift evolution, reddening substantially in both colors by $z \sim 0.5$, as can be seen by the precipitous break in the underlying gray distribution in the middle panel. A similar, but less dramatic trend is seen in the starburst galaxies. To obtain a promising sample of potential active galaxy pairs, we suggest a selection cut at $r - i < 0.8$, which should drastically limit the sample to $z \leqslant 0.5$, regardless of whether the galaxies are star forming or elliptical. Employing this cut on the kinematic pair sample, we recover 62% (18/29) of the galaxies below the redshift threshold, excluding the four galaxies that are at low redshift but lack $r - i$ color data. Based on the SED trends, this color cut will have a slight bias toward selecting lower redshift ellipticals than starbursts. However, the cut does not constrain the redshift of QSOs, which tend to get bluer at higher redshift. A more lenient cut of $r - i < 0.9$ only adds one additional low redshift source while also including four additional high redshift sources, thus lowering the success rate. We note that one of the confirmed dAGNs at low redshift ($0051 + 0020$) significantly fails this color cut, and yet is the most definitive example of a dAGN in our sample. This is because its strong Hα emission line falls within the i band due to its redshift, boosting the color beyond what the smoothed template spectra predict as the reddest color possible for galactic SEDs. The range of $1.50 < r - i < 2.13$ is thus occupied by galaxies with strong emission lines that have been redshifted to $0.095 < z < 0.248$ and could therefore also serve as a useful color preselection. The optical color cut can also be paired with a magnitude cut of $m_r < 20.0$, which yields a similar success rate as the color cut while managing to include the low-z dAGN pair.

Our suggested optical cuts can be used as a preselection criterion for forthcoming large-area surveys. For example, the
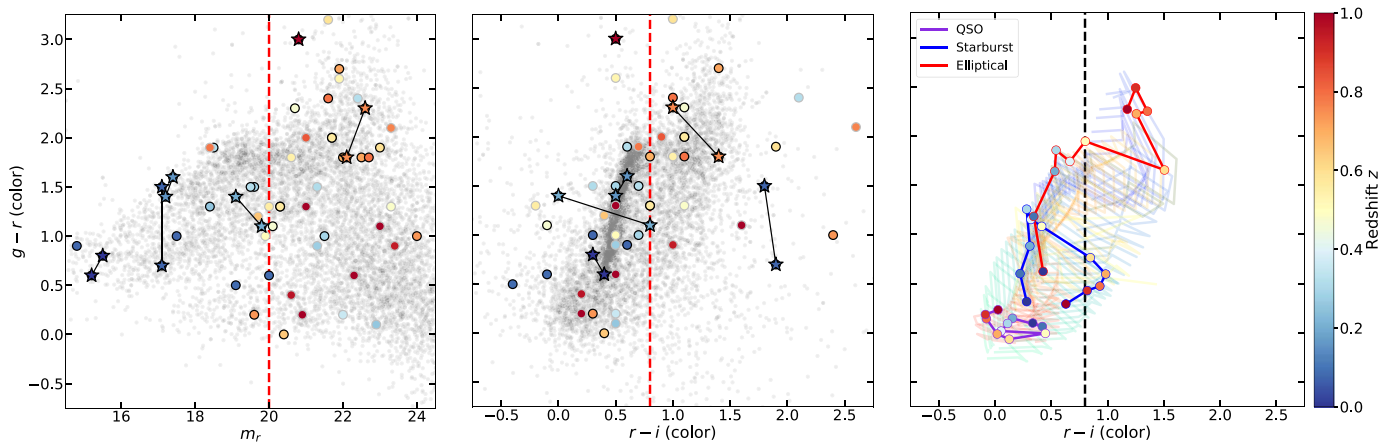
Figure 10. Left: optical color–magnitude diagram for the spectroscopically confirmed pair sample. We plot the apparent r-band magnitude assuming that redshift values would be unknown prior to a spectroscopic follow-up campaign. Galaxies in a kinematic pair are given by black outlined points, stars show the final confirmed dAGN systems (pairs connected by lines), and projected pair galaxies have gray outlines. A magnitude cut of $m_r < 20.0$ (red dashed line) would yield predominantly low-z pairs that have larger angular area and thus would yield fewer jet-aligned pairs via lower resolution radio imaging. Middle: optical color–color diagram. Although there are exceptions, a preselection strategy employing a color cut drawn at $r - i = 0.8$ (red dashed line) would likely yield predominantly low-z pairs. Right: models of redshift evolution of the color–color space for different galaxy classes, at z intervals of 0.1. We highlight three distinct tracks (drawn from the SEDs) which show patterns of differing redshift dependence. QSO spectra are not particularly susceptible to changes in observed colors, while late-type galaxies show a strong dependence on redshift.

Very Large Array Sky Survey (VLASS) began observations in 2017 and will finish its third and final pass in 2024 (Lacy et al. 2020). With observations covering the entire sky north of $\delta > -40°$, the 33,885 deg^2 coverage will overlap entirely with the 14,555 deg^2 of the SDSS imaging survey, including the $\sim$300 deg^2 region of Stripe 82. Only 92 deg^2 of Stripe 82 was covered by the VS82 radio imaging campaign, thus the imaging provided by VLASS can fill in the remainder. We note that this additional 200% area of overlap increase from VLASS will not have equivalent sensitivity ($\sim$70 μJy beam^{-1}) or resolution (2″5) to the VS82 survey (52 μJy beam^{-1}; 1″8). This latter restriction precludes observing any dAGNs with separations under 10 kpc beyond $z \sim 0.26$. On the other hand, even out to $z \sim 0.9$ it should still be possible to resolve dAGNs with sep < 20 kpc. Also, the use of optical cuts once again excludes heavily obscured and dust-reddened dAGN systems; however, these Compton-thick and heavily reddened systems are preferentially found at later merger stages and smaller physical separations (Hickox & Alexander 2018), and thus could be missed by the angular resolution limit of VLASS anyway.

We can roughly estimate the number of sources expected from crossmatching SDSS co-added images with VLASS based on the matching results in Paper I. Of the 17,969 radio sources in the VS82 catalog, 62% were found to have optical matches. Of these, 83 pairs were found with reliable radio source separations within 5″, 52 of which were classified as Grades A and B. Assuming a similar rate of matching for the remaining area of Stripe 82 and taking into account the poorer angular resolution, we would thus expect an additional $\sim$80 such pairs to be found with VLASS in the Stripe 82 field. Given our final census of dAGNs, we might therefore expect to find nine additional dAGN pairs using similar 0″3 radio imaging follow-up, and six dAGNs with only optical signatures.

Gordon et al. (2021) give the first results for the whole area of VLASS using the quicklook image catalog. They note that the quality of VLASS imaging products is well suited for a wide-area search for dAGN, where AGN with radio lobes will

be visible out to $z \sim 0.5$. Our suggested optical color cut would be a complementary preselection strategy to constrain the radio detections to this redshift, enabling an assessment of jet/lobe overlap with companion galaxies. The factor of $\sim$160 increase in the area of the entire SDSS imaging survey over the VS82 region would yield an estimated >9300 pairs designated as Grades A and B using our selection scheme. The coverage of SDSS outside Stripe 82 has $\sim$2 mag shallower observations compared to the co-added catalog of Jiang et al. (2014), lessening the number of optically faint detections. However, the r-band magnitude cut suggested above would still be well above this threshold, so we can estimate the number of pairs that would be selected to be at low redshift. 25% of the Grade A and B pairs would pass this cut, yielding $\sim$1600 new pairs from VLASS. If we ease the restriction so that only one galaxy in the pair needs to pass the cut, this number increases to $\sim$2500 new pairs. Based on the dAGN success rate of our sample, this upper limit should result in $\sim$300 dAGNs, allowing for a robust statistical analysis of the dAGN fraction, incorporating the evolution of the correlated and merger-induced fueling mechanisms with redshift and separation.

5. Summary and Conclusions

We have studied the majority of the remaining Grade A and B samples of candidate dAGNs from Paper I. Optical spectroscopy has revealed that of the 35 pairs observed overall, 21 are found to be kinematic pairs with consistent redshifts and 14 are projected pairs along the line of sight. Spectral fitting offers some indications of LINERS and AGN/star-forming composite systems; however, we find that conclusive BPT classification is significantly hampered by the high redshifts ($z \geqslant 0.47$) for over half of the sample. Our high-resolution 6 GHz VLA radio imaging of 17 kinematic pairs reveals that six (4 previously known and two newly discovered) are indeed bona fide dAGN systems with separate radio core emission. One of these pairs (2319+0038) is at a significantly higher redshift ($z \sim 0.9$), and is more widely separated than the others ($\sim$30 kpc). The remaining 11 kinematic pairs with radio follow-up show a mix of morphologies that suggest the

presence of only one AGN in each system. Many pairs have FR II radio lobes or extended jets originating from one galaxy but are aligned with their companion galaxies, giving the false impression of two separate radio cores at lower angular resolution. This is another complication in the sample selection arising from the high redshift (and thus limited spatial resolution) of the kinematic pairs.

The observed dAGN duty cycle of 0.02% is slightly higher than models of purely stochastic accretion, suggesting some influence of galactic mergers enhancing synchronized black hole activity; however, a larger sample with well-constrained biases is needed to properly address the roles of the different triggering mechanisms and the high fraction of obscured AGN at lower Eddington ratios. In our radio-selected sample, accretion is occurring predominantly at lower levels consistent with radio mode LERGs. We thus suggest that when dAGNs are observable, their triggering is mostly through modest galaxy pair interactions that assist stochastic processes, enhancing accretion levels of LLAGN.

Guided by the complications uncovered in our sample as detailed above, we therefore propose optical cuts for future wide-area surveys, which should preferentially select galaxies at lower redshifts. A color cut at $r - i < 0.8$ selects galaxies mostly below ∼0.5 (corresponding to a separation of 34 kpc for our dAGN with the smallest angular separation), which would then enable BPT optical classification. Similar results could be achieved using an r-band apparent magnitude cut of $m_r < 20.0$. We add these preselection criteria to our original sample selection strategy outlined in Paper I, with the expectation that the revised strategy could yield a sizable population of dAGNs from future and ongoing all-sky surveys such as VLASS. Upon spectroscopic redshift determination, higher-z pairs could also benefit from emission line coverage through JWST, allowing for a complete rest-frame-optical spectra analysis.

In addition to the data included in the online-only journal, data is available upon reasonable request to the corresponding author.

Appendix
Supplemental Tables

Here, we include additional data used in support of the discussion in the main text. These supplemental tables focus only on the kinematic pair sample as is germane to the discussion of validating or refuting dAGN status. Table A1 lists the optical emission line ratios as well as other properties derived from the optical spectra. Table A2 gives the stellar and black hole properties of each galaxy resulting from our spectral fitting analysis. Table A3 gives the results of our various classification schemes used throughout the interpretation of each system, and many of the final classifications are given in the final column of Table 2.

Table A1
Emission Line Properties of the Kinematic Pair Sample

Optical Designation J2000	log([O III]/Hβ)	log([N II]/Hα)	log([S II]/Hα)	log([O I]/Hα)	$L_{Hα}$ log(erg s⁻¹)	$W_{Hα}$ (Å)	$L_{[O III]}$ log(erg s⁻¹)	$P^{int}_{1.4\ GHz}$ log(W Hz⁻¹)
(1)	(2)	(3)	(4)	(5)	(6)	(7)	(8)	(9)
005113.93+002047.2	0.1 ± 0.03	−0.18 ± 0.03	−0.39 ± 0.05	−1.16 ± 1.25	41.1	1.5 ± 0.0	40.4	22.3
005114.11+002049.4	−0.36 ± 0.26	−0.23 ± 0.0	−0.42 ± 0.0	−1.35 ± 0.72	41.4	1.8 ± 0.0	40.1	23.1
013412.78−010729.5	0.56 ± 0.02	0.42 ± 0.04	0.13 ± 0.09	⋯ ± ⋯	40.1	0.1 ± 0.5	40.1	23.1
013412.84−010725.0	0.09 ± 0.0	−0.1 ± 0.0	0.39 ± 0.0	−0.7 ± 0.02	39.0	−0.5 ± 0.0	38.8	23.0
014203.08−000150.3	⋯ ± ⋯	⋯ ± ⋯	⋯ ± ⋯	⋯ ± ⋯	⋯	⋯ ± ⋯	⋯	24.0
014203.24−000151.0	0.4 ± 0.03	⋯ ± ⋯	⋯ ± ⋯	⋯ ± ⋯	⋯	⋯ ± ⋯	41.0	25.0
014715.86−000819.5	−0.18 ± 0.0	⋯ ± ⋯	⋯ ± ⋯	⋯ ± ⋯	⋯	⋯ ± ⋯	40.5	24.1
014715.94−000817.4	0.22 ± 0.07	⋯ ± ⋯	⋯ ± ⋯	⋯ ± ⋯	⋯	⋯ ± ⋯	41.9	24.2
014928.38−001446.0	0.35 ± 0.08	−0.84 ± 0.25	−0.29 ± 0.07	−1.14 ± 0.49	39.5	1.4 ± 0.0	39.2	22.6
014928.41−001447.8	0.19 ± 0.13	−1.62 ± 1.88	−0.33 ± 0.1	−0.8 ± 0.25	39.2	1.1 ± 0.0	38.9	22.4
015253.79−001005.6	⋯ ± ⋯	0.2 ± 0.03	0.11 ± 0.03	−1.24 ± 0.68	39.9	0.1 ± 0.1	39.1	22.7
015253.92−001004.3	−0.27 ± 0.01	0.05 ± 0.11	0.04 ± 0.11	−0.4 ± 0.22	39.0	−0.0 ± 0.2	38.3	21.9
020301.40−003341.7	−0.34 ± 0.25	⋯ ± ⋯	⋯ ± ⋯	⋯ ± ⋯	⋯	⋯ ± ⋯	40.3	24.7
020301.43−003339.3	0.37 ± 0.13	⋯ ± ⋯	⋯ ± ⋯	⋯ ± ⋯	⋯	⋯ ± ⋯	40.9	24.5
021021.00−005124.2	⋯ ± ⋯	0.08 ± 0.0	0.52 ± 0.0	⋯ ± ⋯	39.6	−0.5 ± 0.0	39.6	23.8
021021.13−005126.7	0.48 ± 0.0	−0.68 ± 0.79	−0.1 ± 0.21	−1.08 ± 2.0	40.2	0.9 ± 0.0	39.7	23.8
220634.97+000327.6	−0.05 ± 0.07	−0.13 ± 0.02	−0.16 ± 0.03	−1.05 ± 0.97	40.4	1.1 ± 0.0	39.8	22.0
220635.08+000323.3	0.22 ± 0.02	0.13 ± 0.0	0.12 ± 0.0	−0.5 ± 0.05	40.7	1.3 ± 0.0	40.3	22.1
221142.42+002731.2	−0.56 ± 0.16	⋯ ± ⋯	⋯ ± ⋯	⋯ ± ⋯	⋯	⋯ ± ⋯	39.4	25.3
221142.51+002728.5	−0.54 ± 0.14	⋯ ± ⋯	⋯ ± ⋯	⋯ ± ⋯	⋯	⋯ ± ⋯	41.9	25.5
222051.55+005815.5	−0.28 ± 0.0	0.75 ± 0.02	0.37 ± 0.05	⋯ ± ⋯	40.0	−0.2 ± 0.0	40.0	24.7
222051.70+005816.7	⋯ ± ⋯	1.01 ± 0.0	1.02 ± 0.0	⋯ ± ⋯	38.9	−0.9 ± 0.0	39.7	25.1
222907.53−000411.1	0.43 ± 0.0	⋯ ± ⋯	⋯ ± ⋯	⋯ ± ⋯	⋯	⋯ ± ⋯	40.8	25.2
222907.77−000410.9	⋯ ± ⋯	⋯ ± ⋯	⋯ ± ⋯	⋯ ± ⋯	⋯	⋯ ± ⋯	36.9	24.9
223222.41+001226.3	0.08 ± 0.14	−0.25 ± 0.04	−0.36 ± 0.05	−1.12 ± 1.48	41.2	1.5 ± 0.0	39.9	22.9
223222.60+001224.7	−0.21 ± 0.27	−0.35 ± 0.0	−0.38 ± 0.0	−1.31 ± 3.37	41.2	1.6 ± 0.0	39.8	23.2
223546.28+000358.8	⋯ ± ⋯	⋯ ± ⋯	⋯ ± ⋯	⋯ ± ⋯	⋯	⋯ ± ⋯	⋯	25.0
223546.40+000358.7	⋯ ± ⋯	⋯ ± ⋯	⋯ ± ⋯	⋯ ± ⋯	⋯	⋯ ± ⋯	⋯	24.2
224426.44+001051.3	0.26 ± 0.0	⋯ ± ⋯	⋯ ± ⋯	⋯ ± ⋯	⋯	⋯ ± ⋯	40.6	24.6
224426.61+001051.9	0.16 ± 0.11	⋯ ± ⋯	⋯ ± ⋯	⋯ ± ⋯	⋯	⋯ ± ⋯	40.8	25.0
224532.53+005857.9	0.66 ± 0.01	⋯ ± ⋯	⋯ ± ⋯	⋯ ± ⋯	⋯	⋯ ± ⋯	41.2	24.5
224532.68+005855.8	0.48 ± 0.03	⋯ ± ⋯	⋯ ± ⋯	⋯ ± ⋯	⋯	⋯ ± ⋯	41.6	24.1
225222.52+010658.0	0.08 ± 0.05	0.54 ± 0.04	0.48 ± 0.04	−0.21 ± 0.24	40.1	0.1 ± 0.4	40.7	22.4
225222.65+010700.6	−0.44 ± 0.21	−0.39 ± 0.0	−0.55 ± 0.0	−1.67 ± 7.7	40.7	1.7 ± 0.0	39.5	21.9
225817.73+003007.7	⋯ ± ⋯	⋯ ± ⋯	⋯ ± ⋯	⋯ ± ⋯	⋯	⋯ ± ⋯	39.2	23.4
225817.97+003011.5	−0.15 ± 0.16	−0.69 ± 0.9	−0.52 ± 0.62	−1.45 ± 2.43	40.6	1.3 ± 0.0	39.8	24.3
230010.18−000531.7	−0.4 ± 0.0	0.38 ± 0.04	−0.03 ± 0.09	⋯ ± ⋯	40.2	0.1 ± 0.3	39.8	23.2
230010.24−000534.0	−0.59 ± 0.37	⋯ ± ⋯	⋯ ± ⋯	⋯ ± ⋯	⋯	⋯ ± ⋯	39.9	23.0
230342.74−011712.7	−0.37 ± 0.39	⋯ ± ⋯	⋯ ± ⋯	⋯ ± ⋯	⋯	⋯ ± ⋯	40.1	24.4
230342.91−011711.9	−0.07 ± 0.0	⋯ ± ⋯	⋯ ± ⋯	⋯ ± ⋯	⋯	⋯ ± ⋯	40.5	24.6
231953.31+003816.7	⋯ ± ⋯	⋯ ± ⋯	⋯ ± ⋯	⋯ ± ⋯	⋯	⋯ ± ⋯	⋯	25.3
231953.43+003813.4	⋯ ± ⋯	⋯ ± ⋯	⋯ ± ⋯	⋯ ± ⋯	⋯	⋯ ± ⋯	⋯	24.6

Note. Every two rows is a pair, and sources are sorted in ascending R.A. (1) J2000 coordinate of the optical source; (2)−(5) logarithmic emission line ratios and 1σ errors; (6) logarithmic Hα luminosity; (7) Hα equivalent width and 1σ error; (8) logarithmic [O III] luminosity; (9) logarithmic radio power computed from integrated source flux at 1.4 GHz.

Table A2
Derived Optical Properties of Kinematic Pair Sample

Optical Designation J2000 (1)	$M_\star$ log($M_\odot$) (2)	$\sigma_\star$ (km s^{-1}) (3)	M_{BH} log($M_\odot$) (4)	log(λ_{Edd}) (5)
005113.93+002047.2	10.3	150.0*	7.9	−2.0
005114.11+002049.4	10.5	173.78*	8.1	−2.4
013412.78-010729.5	11.3	278.48	9.0	−3.3
013412.84-010725.0	10.6	225.26	8.2	−3.1
014203.08-000150.3	10.9	⋯	8.6	−2.8
014203.24-000151.0	11.4	234.13	9.2	−2.4
014715.86-000819.5	11.4	⋯	9.1	−2.9
014715.94-000817.4	10.4	646.26	8.0	−0.6
014928.38-001446.0	9.1	⋯	6.5	−1.5
014928.41-001447.8	9.0	⋯	6.4	−1.6
015253.79-001005.6	10.9	⋯	8.6	−3.5
015253.92-001004.3	10.2	⋯	7.7	−3.3
020301.40-003341.7	10.1	⋯	7.7	−1.3
020301.43-003339.3	10.0	⋯	7.6	−1.0
021021.00-005124.2	11.2	⋯	9.0	−3.2
021021.13-005126.7	10.2	⋯	7.7	−2.0
220634.97+000327.6	10.1	124.45*	7.6	−2.3
220635.08+000323.3	10.4	180.03*	7.9	−2.2
221142.42+002731.2	10.9	⋯	8.6	−1.9
221142.51+002728.5	12.1	202.3	9.9	−2.5
222051.55+005815.5	11.2	357.58	8.9	−2.6
222051.70+005816.7	10.9	350.46	8.6	−2.1
222907.53-000411.1	11.6	250.83	9.4	−2.7
222907.77-000410.9	10.9	⋯	8.6	−2.2
223222.41+001226.3	10.0	195.63*	7.5	−2.0
223222.60+001224.7	10.2	170.51*	7.7	−2.2
223546.28+000358.8	11.8	235.34	9.6	⋯
223546.40+000358.7	11.4	280.15	9.2	⋯
224426.44+001051.3	11.1	⋯	8.9	−2.4
224426.61+001051.9	10.0	⋯	7.5	−0.9
224532.53+005857.9	10.2	274.69	7.7	−0.9
224532.68+005855.8	11.0	⋯	8.6	−1.6
225222.52+010658.0	10.8	258.57	8.4	−2.3
225222.65+010700.6	9.4	214.67	6.9	−1.8
225817.73+003007.7	11.3	⋯	9.1	−3.7
225817.97+003011.5	9.8	450.88	7.3	−1.3
230010.18-000531.7	11.3	318.78*	9.1	−3.6
230010.24-000534.0	11.4	347.85*	9.2	−3.6
230342.74-011712.7	11.5	283.87	9.3	−3.1
230342.91-011711.9	11.5	234.26	9.3	−2.9
231953.31+003816.7	11.9	⋯	9.7	⋯
231953.43+003813.4	12.0	⋯	9.8	⋯

Note. Every two rows is a pair, and sources are sorted in ascending R.A. (1) J2000 coordinate of the optical source; (2) stellar mass measured from modeling the optical spectrum with SSPs; (3) intrinsic stellar velocity dispersion of the stellar populations, where the higher resolution SDSS spectra are marked with *; (4) black hole mass inferred from the $M_\bullet$–M_{bulge} relation of Kormendy & Ho (2013), which has an intrinsic scatter of ∼0.29 dex; (5) Eddington ratio, $\lambda_{Edd} = (L_{rad} + L_{mech})/L_{Edd}$.

Table A3
AGN Classifications of the Kinematic Pair Sample

Optical Designation J2000 (1)	BPT1 Class (2)	BPT2 Class (3)	BPT3 Class (4)	Radio Excess (5)	Radio Loud (6)	MIR Color (7)	Mode (8)
005113.93+002047.2	Comp	SF	Seyfert	✓	×	✓	L
005114.11+002049.4	Comp	SF	SF	✓	×	✓	L
013412.78-010729.5	LINER	LINER	…	✓	×	×	L
013412.84-010725.0	Comp	LINER	LINER	✓	✓	×	L
014203.08-000150.3	…	…	…	♡	✓	×	L
014203.24-000151.0	…	…	…	♡	✓	×	L
014715.86-000819.5	…	…	…	♡	✓	×	L
014715.94-000817.4	…	…	…	♡	×	×	H
014928.38-001446.0	SF	Seyfert	Seyfert	✓	×	×	H
014928.41-001447.8	SF	SF	LINER	✓	×	×	H
015253.79-001005.6	…	…	…	✓	×	×	L
015253.92-001004.3	LINER	LINER	LINER	✓	×	×	L
020301.40-003341.7	…	…	…	♡	✓	×	H
020301.43-003339.3	…	…	…	♡	✓	×	H
021021.00-005124.2	…	…	…	✓	✓	×	L
021021.13-005126.7	Comp	LINER	Seyfert	✓	✓	×	H
220634.97+000327.6	Comp	LINER	LINER	✓	×	×	L
220635.08+000323.3	LINER	LINER	LINER	✓	×	×	L
221142.42+002731.2	…	…	…	♡	✓	✓	L
221142.51+002728.5	…	…	…	♡	✓	✓	H
222051.55+005815.5	LINER	LINER	…	✓	✓	×	L
222051.70+005816.7	…	…	…	✓	✓	×	L
222907.53-000411.1	…	…	…	♡	✓	×	H
222907.77-000410.9	…	…	…	×	×	×	L
223222.41+001226.3	Comp	SF	Seyfert	✓	×	✓	L
223222.60+001224.7	Comp	SF	SF	✓	✓	✓	L
223546.28+000358.8	…	…	…	♡	×	×	…
223546.40+000358.7	…	…	…	×	×	×	…
224426.44+001051.3	…	…	…	♡	✓	×	L
224426.61+001051.9	…	…	…	♡	✓	×	H
224532.53+005857.9	…	…	…	♡	✓	✓	H
224532.68+005855.8	…	…	…	♡	×	✓	H
225222.52+010658.0	LINER	LINER	LINER	✓	×	×	L
225222.65+010700.6	SF	SF	SF	✓	×	×	L
225817.73+003007.7	…	…	…	×	✓	✓	L
225817.97+003011.5	SF	SF	SF	✓	✓	✓	L
230010.18-000531.7	LINER	LINER	…	✓	✓	×	L
230010.24-000534.0	…	…	…	♡	×	×	L
230342.74-011712.7	…	…	…	♡	✓	×	L
230342.91-011711.9	…	…	…	♡	✓	×	L
231953.31+003816.7	…	…	…	×	×	×	…
231953.43+003813.4	…	…	…	×	×	×	…

Note. Every two rows is a pair, and sources are sorted in ascending R.A. (1) J2000 coordinate of the optical source; (2)–(4) BPT diagnostic classifications; (5) Radio excess determined via Hα SFR (♡ denotes radio excess via Balmer decrement); (6) Radio loudness determined via $L_{[O\ III]}$; (7) MIR color AGN status based on criteria of Satyapal et al. (2017); (8) mode of AGN activity (HERG/LERG) based on criteria of Best & Heckman (2012).

ORCID iDs

Arran C. Gross ⬡ https://orcid.org/0000-0001-7681-9213
Hai Fu ⬡ https://orcid.org/0000-0001-9608-6395
S. G. Djorgovski ⬡ https://orcid.org/0000-0002-0603-3087
Joshua L. Steffen ⬡ https://orcid.org/0000-0003-3299-9595
J. M. Wrobel ⬡ https://orcid.org/0000-0001-9720-7398

References

Ahn, C. P., Alexandroff, R., Allende Prieto, C., et al. 2014, ApJS, 211, 17
Baldry, I. K., Driver, S. P., Loveday, J., et al. 2012, MNRAS, 421, 621
Baldwin, J. A., Phillips, M. M., & Terlevich, R. 1981, PASP, 93, 5
Bariuan, L. G. C., Snios, B., Sobolewska, M., Siemiginowska, A., & Schwartz, D. A. 2022, MNRAS, 513, 4673
Barnes, J. E., & Hernquist, L. 1996, ApJ, 471, 115
Barnes, J. E., & Hernquist, L. E. 1991, ApJL, 370, L65
Best, P. N., & Heckman, T. M. 2012, MNRAS, 421, 1569
Blecha, L., Loeb, A., & Narayan, R. 2013, MNRAS, 429, 2594
Buttiglione, S., Capetti, A., Celotti, A., et al. 2010, A&A, 509, A6
Calzetti, D., Armus, L., Bohlin, R. C., et al. 2000, ApJ, 533, 682
Capelo, P. R., & Dotti, M. 2016, MNRAS, 465, 2643
Capelo, P. R., Dotti, M., Volonteri, M., et al. 2017, MNRAS, 469, 4437
Cappellari, M., & Emsellem, E. 2004, PASP, 116, 138
Cardelli, J. A., Clayton, G. C., & Mathis, J. S. 1989, ApJ, 345, 245
Cavagnolo, K. W., McNamara, B. R., Nulsen, P. E. J., et al. 2010, ApJ, 720, 1066
Cid Fernandes, R., Stasińska, G., Mateus, A., & Vale Asari, N. 2011, MNRAS, 413, 1687
Condon, J. J. 1997, PASP, 109, 166
Dawson, K. S., Schlegel, D. J., Ahn, C. P., et al. 2013, AJ, 145, 10
De Rosa, A., Vignali, C., Bogdanović, T., et al. 2019, NewAR, 86, 101525
Di Matteo, T., Springel, V., & Hernquist, L. 2005, Natur, 433, 604
Ellison, S. L., Patton, D. R., Simard, L., & McConnachie, A. W. 2008, AJ, 135, 1877
Fanaroff, B. L., & Riley, J. M. 1974, MNRAS, 167, 31P
Fu, H., Myers, A. D., Djorgovski, S. G., et al. 2015a, ApJ, 799, 72
Fu, H., Steffen, J. L., Gross, A. C., et al. 2018, ApJ, 856, 93
Fu, H., Wrobel, J. M., Myers, A. D., Djorgovski, S. G., & Yan, L. 2015b, ApJL, 815, L6
Fu, H., Zhang, Z.-Y., Assef, R. J., et al. 2011, ApJL, 740, L44
Gordon, Y. A., Boyce, M. M., O'Dea, C. P., et al. 2021, ApJS, 255, 30
Goulding, A. D., Greene, J. E., Bezanson, R., et al. 2018, PASJ, 70, S37
Goulding, A. D., Pardo, K., Greene, J. E., et al. 2019, ApJL, 879, L21
Gross, A. C., Fu, H., Myers, A. D., Wrobel, J. M., & Djorgovski, S. G. 2019, ApJ, 883, 50
Heckman, T. M., & Best, P. N. 2014, ARA&A, 52, 589
Heckman, T. M., Kauffmann, G., Brinchmann, J., et al. 2004, ApJ, 613, 109
Hickox, R. C., & Alexander, D. M. 2018, ARA&A, 56, 625
Hopkins, A. M., McClure-Griffiths, N. M., & Gaensler, B. M. 2008, ApJL, 682, L13
Hopkins, P. F., Hernquist, L., Cox, T. J., et al. 2006, ApJL, 163, 1
Hou, M., Li, Z., & Liu, X. 2020, ApJ, 900, 79
Ilbert, O., Capak, P., Salvato, M., et al. 2008, ApJ, 690, 1236
Ilbert, O., Salvato, M., Le Floc'h, E., et al. 2010, ApJ, 709, 644
Jarrett, T. H., Cohen, M., Masci, F., et al. 2011, ApJ, 735, 112
Jiang, L., Fan, X., Bian, F., et al. 2014, ApJS, 213, 12
Kauffmann, G., & Heckman, T. M. 2009, MNRAS, 397, 135
Kauffmann, G., Heckman, T. M., Tremonti, C., et al. 2003, MNRAS, 346, 1055
Kellermann, K. I., Sramek, R., Schmidt, M., Shaffer, D. B., & Green, R. 1989, AJ, 98, 1195
Kewley, L. J., Dopita, M. A., Sutherland, R. S., Heisler, C. A., & Trevena, J. 2001, ApJ, 556, 121
Kewley, L. J., Groves, B., Kauffmann, G., & Heckman, T. 2006, MNRAS, 372, 961
Kormendy, J., & Ho, L. C. 2013, ARA&A, 51, 511
Koss, M., Mushotzky, R., Veilleux, S., et al. 2011, ApJL, 735, L42
Koss, M. J., Blecha, L., Bernhard, P., et al. 2018, Natur, 563, 214
Lacy, M., Baum, S. A., Chandler, C. J., et al. 2020, PASP, 132, 035001
Laloux, B., Georgakakis, A., Andonie, C., et al. 2022, MNRAS, 518, 2546
Li, K., Ballantyne, D. R., & Bogdanović, T. 2021, ApJ, 916, 110
Markwardt, C. B. 2009, in ASP Conf. Ser. 411, Astronomical Data Analysis Software and Systems XVIII, ed. D. A. Bohlender, D. Durand, & P. Dowler (San Francisco, CA: ASP), 251
Merloni, A., Bongiorno, A., Brusa, M., et al. 2014, MNRAS, 437, 3550
Merloni, A., Heinz, S., & Matteo, T. D. 2005, Ap&SS, 300, 45
Murphy, E. J., Condon, J. J., Schinnerer, E., et al. 2011, ApJ, 737, 67
Oke, J. B., Cohen, J. G., Carr, M., et al. 1995, PASP, 107, 375
Osterbrock, D. E., & Ferland, G. J. 2006, Astrophysics of Gaseous Nebulae and Active Galactic Nuclei (2nd ed.; Sausalito, CA: Univ. Science Books)
Perley, D. A. 2019, PASP, 131, 084503
Perley, R. A., & Butler, B. J. 2013, ApJL, 204, 19
Pfeifle, R. W., Satyapal, S., Manzano-King, C., et al. 2019, ApJ, 883, 167
Pillepich, A., Nelson, D., Hernquist, L., et al. 2017, MNRAS, 475, 648
Polletta, M., Tajer, M., Maraschi, L., et al. 2007, ApJ, 663, 81
Ricci, C., Ananna, T. T., Temple, M. J., et al. 2022, ApJ, 938, 67
Ricci, C., Privon, G. C., Pfeifle, R. W., et al. 2021, MNRAS, 506, 5935
Ricci, C., Trakhtenbrot, B., Koss, M. J., et al. 2017, Natur, 549, 488
Robotham, A. S. G., Driver, S. P., Davies, L. J. M., et al. 2014, MNRAS, 444, 3986
Rodriguez-Gomez, V., Pillepich, A., Sales, L. V., et al. 2016, MNRAS, 458, 2371
Rosas-Guevara, Y. M., Bower, R. G., McAlpine, S., Bonoli, S., & Tissera, P. B. 2019, MNRAS, 483, 2712
Roy, N., Moravec, E., Bundy, K., et al. 2021, ApJ, 922, 230
Salvato, M., Hasinger, G., Ilbert, O., et al. 2008, ApJ, 690, 1250
Sanders, D. B., Soifer, B. T., Elias, J. H., et al. 1988, ApJ, 325, 74
Satyapal, S., Secrest, N. J., Ricci, C., et al. 2017, ApJ, 848, 126
Scudder, J. M., Ellison, S. L., Torrey, P., Patton, D. R., & Mendel, J. T. 2012, MNRAS, 426, 549
Shabala, S. S., Ash, S., Alexander, P., & Riley, J. M. 2008, MNRAS, 388, 625
Shankar, F., Weinberg, D. H., & Miralda-Escudé, J. 2008, ApJ, 690, 20
Shen, Y., Chen, Y.-C., Hwang, H.-C., et al. 2021, NatAs, 5, 569
Singha, M., O'Dea, C. P., Gordon, Y. A., Lawlor-Forsyth, C., & Baum, S. A. 2021, ApJ, 918, 65
Steffen, J. L., Fu, H., Brownstein, J. R., et al. 2023, ApJ, 942, 107
Steffen, J. L., Fu, H., Comerford, J. M., et al. 2021, ApJ, 909, 120
Thomas, D., Steele, O., Maraston, C., et al. 2013, MNRAS, 431, 1383
Torrey, P., Vogelsberger, M., Sijacki, D., Springel, V., & Hernquist, L. 2012, MNRAS, 427, 2224
Tubín, D., Treister, E., D'Ago, G., et al. 2021, ApJ, 911, 100
Vazdekis, A., Ricciardelli, E., Cenarro, A. J., et al. 2012, MNRAS, 424, 157
Volonteri, M., Pfister, H., Beckmann, R., et al. 2022, MNRAS, 514, 640
Wassenhove, S. V., Volonteri, M., Mayer, L., et al. 2012, ApJL, 748, L7
Weigel, A. K., Schawinski, K., Treister, E., Trakhtenbrot, B., & Sanders, D. B. 2018, MNRAS, 476, 2308
Wright, E. L., Eisenhardt, P. R. M., Mainzer, A. K., et al. 2010, AJ, 140, 1868
Xu, C., Livio, M., & Baum, S. 1999, AJ, 118, 1169
Yang, X., Ji, J., Joshi, R., et al. 2022, ApJ, 933, 98
Yue, M., Fan, X., Yang, J., & Wang, F. 2021, ApJL, 921, L27
Yun, M. S., Reddy, N. A., & Condon, J. J. 2001, ApJ, 554, 803
Zhang, Y.-W., Huang, Y., Bai, J.-M., et al. 2021a, AJ, 162, 289
Zhang, Y.-W., Huang, Y., Bai, J.-M., et al. 2021b, AJ, 162, 276